[This is a non-peer-reviewed preprint submitted to EarthArXiv and currently under review in the journal Earth and Planetary Science Letters]

Astronomical pacing of the Ludfordian Biogeochemical Event, the largest carbon cycle perturbation of the Phanerozoic

Michiel Arts[1]

Damien Pas[1,2]

Jiří Frýda[3,4]

Anne-Christine da Silva[1]

1 - SEDICLIM lab, Department of Geology, University of Liege, Liege, Belgium

2 - Institute of Earth Sciences (ISTE), University of Lausanne, Lausanne, Switzerland

3 - Faculty of Environmental Sciences, Czech University of Life Sciences, Prague, Czech Republic

4 - Czech Geological Survey, Prague 1, Czech Republic

Corresponding author: Michiel Arts, michiel.arts@uliege.

Present address: University of Liege, Allee du Six Aout 12, B20, 4000 Liège, Belgium

ORCID

Michiel Arts https://orcid.org/0000-0003-3181-4608

Damien Pas https://orcid.org/0000-0002-2235-1974

Jiří Frýda https://orcid.org/0000-0003-2410-3293

Da Silva Anne-Christine https://orcid.org/0000-0003-4191-7600

Keywords: Ludfordian Biogeochemical Event, astrochronology, carbon cycle dynamics, glacio-eustasy, ocean circulation

Abstract

The Kosov Quarry section (Prague Basin, Czech Republic) preserves one of the most complete Silurian successions spanning the Ludfordian (late Silurian) Biogeochemical Event (LBE), encompassing the mid-Ludfordian Carbon Isotope Excursion (MLCIE), the largest positive $\delta^{13}C_{carb}$ excursion of the Phanerozoic. The LBE is associated with climatic cooling, redox reorganisation, sea-level change, and faunal turnover, yet its tempo and driving mechanisms have remained poorly constrained. Here, we establish an anchored astrochronology for the Kosov Quarry succession based on lithological induration patterns and anchored to the Ludfordian–Pridoli boundary. The resulting age model resolves astronomical cycles from half-precession (~8.5 kyr) to 405-kyr eccentricity cycle and constrains the onset of the LBE to 424.30 ± 0.60 Ma, with a total duration of 1.15 ± 0.26 Myr. The Lau–Kozłowskii Bioevent, representing a brief extinction pulse during the culmination of the Siluricus ocean anoxic event just before the MLCIE, lasted 30 ± 10 kyr. Spectral and phase analyses reveal a strong imprint of the eccentricity cycles in the induration, lag-1 sea-level, and $\delta^{13}C_{carb}$ rate-of-change (‰/kyr) records. Phase relationships indicate that the sea level was subjected to a glacio-eustatic regime. The $\delta^{13}C_{carb}$ change rate reached up to 0.09 (‰/kyr), implying rapid carbon burial during eccentricity minima, transient CO_2 drawdown, and possible glacial expansion. These results demonstrate that eccentricity pacing exerted a first-order control on Silurian carbon-cycle feedbacks and sea-level change. Our astrochronology provides the first high-resolution temporal calibration of the entire LBE and a quantitative framework for integrating astronomical forcing into Palaeozoic carbon-cycle perturbations.

1. Introduction

Understanding large-scale carbon cycle perturbations is crucial, as they provide insights into the feedbacks that govern Earth's climate system and the thresholds beyond which these feedbacks can drive nonlinear or runaway climate responses (Berner, 2004; Gregory et al., 2009; Zeebe and Ridgwell, 2011; Isson et al., 2020). These feedbacks are mediated through changes in carbon partitioning among the atmosphere, ocean, and biosphere, which directly regulate global temperature, ocean chemistry, and redox structure. As a result, carbon redistribution influences both the onset of environmental collapse and its recovery (Cramer and Jarvis, 2020). While tectonic and volcanic processes dominate multimillion-year trends, on timescales of 10^3–10^6 years, the system is sensitive to astronomically driven variations in insolation, hydrology, and organic carbon burial (Calvert and Pedersen, 1992; Hinnov, 2018; Laurin et al., 2015; Laurin et al., 2017).

Astronomical theory posits that cyclic variations in the Earth's astronomical parameters (eccentricity, obliquity, and precession) alter the distribution and intensity of solar radiation received at the surface, leading to periodic changes in climate and oceanographic circulation (Hays et al., 1976; Hinnov and Hilgen, 2012). The global carbon cycle can respond to astronomical forcing through shifts in weathering, nutrient delivery, primary productivity, and the preservation of organic carbon in sediments (De Vleeschouwer et al., 2020; Ma et al., 2011; Vervoort et al., 2024). Although astronomical forcing's imprint on carbon burial and geochemical redox cycles is well-documented (Gambacorta et al., 2016; Huang et al., 2021; Laurin et al., 2015; Li et al., 2024), its

strength and expression across Pre-Cenozoic biogeochemical events remain poorly constrained (De Vleeschouwer et al., 2024).

The Silurian Period is marked by recurrent environmental instabilities and accompanying extinctions–recovery cycles (Calner, 2008; Melchin et al., 2020; Štorch, 1995), accompanied by some of the largest carbon-cycle perturbations of the Phanerozoic, with $\delta^{13}C$ excursions ranking among the highest of the entire era (Cramer and Jarvis, 2020; Claussen et al., 2024; Melchin et al., 2020; Saltzman, 2005). Notably, extinction rates during Silurian events were comparatively modest, implying a coupling among climate, ocean circulation, the carbon cycle, and life that is not commonly observed (Calner, 2008; Li et al., 2021).

A longstanding paradox is that many Silurian positive $\delta^{13}C$ excursions coincide with a shift toward reefal and carbonate-platform facies rather than widespread organic-rich anoxic shale deposits as typically observed in other parts of the Phanerozoic (Aldridge et al., Becker et al., 2020; Cramer and Saltzman, 2007a, 2007b; Emeis and Weissert, 2009; Jeppsson 1993; Jeppsson, 1990; Jeppsson et al., 1995; Munnecke et al., 2003; Ohkouchi et al., 2015). To reconcile mismatch between large-amplitude $\delta^{13}C$ excursions and geological record, several conceptual models have been developed with the earliest and most influential being the P–S state model that proposes that oscillations between low latitude humid, low-$\delta^{13}C$ P-state (enhanced runoff, marl deposition, and circulation promoting $\delta^{13}C$-depleted deep-water influence) and low latitude arid, high-$\delta^{13}C$ S-state (reduced runoff, enhanced carbonate production and reef growth, and a reorganized circulation favouring stratification and deep-water oxygen depletion). Transitions from P- to S-state are proposed to act as a nonlinear amplifying mechanism for Silurian $\delta^{13}C$

141 excursions (Bickert et al., 1997; Cramer, 2007a, 2007b; Jeppsson, 1990; Munnecke et
142 al., 2010). However, this one and alternative models remain largely conceptual and basin-
143 specific, with poorly constrained temporal relationships to sea level, temperature, and
144 astronomical forcing, compounded by the low precision of the Silurian timescale (Melchin
145 et al., 2020). As a result, the pacing, rates, and amplification mechanisms of Silurian
146 carbon-cycle perturbations remain unresolved, highlighting the need for integrative
147 stratigraphic, geochemical, and astrochronological approaches.

148 The Ludfordian Biogeochemical Event (LBE) represents the most extreme carbon-cycle
149 disruption of the Phanerozoic Eon, culminating in the mid-Ludfordian Carbon Isotope
150 Excursion (MLCIE), reaching $\delta^{13}C_{carb}$ values of 8–12‰ (Cramer and Jarvis, 2020). The
151 LBE was accompanied by a faunal turnover, temperature and sea-level changes, and
152 redox fluctuations (Calner, 2005; Calner and Eriksson, 2006; Calner, 2008; del Rey et al.,
153 2023; Frýda and Manda, 2013; Frýda et al., 2020; Kozłowski and Sobień, 2012; Trotter
154 et al., 2016; Sproson, 2020; Zhang et al., 2022). Crucially, the LBE exemplifies the
155 Silurian paradox, making it a critical test case for evaluating climate models, such as the
156 impact of astronomically paced climate forcing on large-amplitude $\delta^{13}C_{carb}$ excursions
157 amplified by circulation-state transitions, or simply resulting from localised organic-carbon
158 accumulation. Furthermore, the LBE also offers a unique opportunity to assess whether
159 large-amplitude $\delta^{13}C$ excursions reflect astronomically paced climate forcing amplified by
160 circulation-state transitions, or simply resulting from localised organic-carbon
161 accumulation. Despite its global expression and conceptual importance, the duration,
162 tempo, and internal structure of the LBE remain poorly constrained, as most existing
163 interpretations rely on low-resolution or imprecise time scales. Resolving whether the LBE

represents a short-lived perturbation or a prolonged interval of instability, and whether proposed climatic transitions were abrupt, gradual, or astronomically paced, requires a robust astrochronological framework capable of quantifying rates of environmental and carbon-cycle change.

Here, we conduct a high-resolution cyclostratigraphic analysis of the Kosov quarry section, which provides a nearly continuous sedimentary archive across the LBE. We use the induration record of Frýda et al. (2020) as the primary proxy for astrochronological tuning, thereby enabling the estimation of durations and associated uncertainties for the LBE and its subintervals. Based on the tuned induration record, we derive a lag-1 sea-level proxy to assess sea-level variability and calculate rates of change in the $\delta^{13}C_{carb}$ record (‰/kyr). We then evaluate the astronomical imprint and phasing in lithological, geochemical, and sea-level proxies to constrain the pacing of carbon burial and remineralisation, the coupling between sea-level change and $\delta 13C_{carb}$ perturbations, and the role of astronomical forcing in modulating carbon-cycle feedbacks during the LBE.

2. Geological setting

This study focuses on the upper Silurian (Ludfordian) succession of the Kosov quarry, located in the Prague Basin of the Czech Republic (Fig. 1A-B). This basin forms part of the Barrandian (Teplá-Barrandian terrane) within the larger Bohemian Massif (Frýda and Manda, 2013; Frýda et al., 2021, 2020). During the Ludfordian, the terrane was positioned at ~25–30°S (Scotese, 2021; Tasáryová et al., 2014), and deposition occurred in a hemipelagic setting within an intra-plate linear rift basin divided into several sub-basins

(Horný, 1955; Kříž, 1991). The tectonic affinity of the Barrandian terrane remains debated, with it being either a peri-Gondwanan fragment or its own isolated Perunica microcontinent (Fatka and Mergl, 2009).

The studied Kosov section (No. JF195; 49°56′12.2″N, 14°03′20.1″E) provides one of the most complete global records of the Ludfordian Biogeochemical Event (LBE), including the Lau/Kozlowskii Bioevent (LKB), the mid-Ludfordian Carbon Isotope Excursion (MLCIE), and a mid-Ludfordian Glaciation, all integral parts of the LBE (Frýda et al., 2021, 2020; Frýda and Manda, 2013) (Fig. 2 G, H, J). The succession comprises carbonates with marly interbeds and shales, including micritic mudstones, skeletal limestones, and crinoidal grainstones (Kříž, 1992; Lehnert et al., 2007a) (Fig. 1C). The site has been widely studied for its sedimentology, palaeontology, geochemical and faunal changes across the LKB and MLCIE (del Rey et al., 2023; Farkaš et al., 2016, 2024; Frýda et al., 2020, 2021; Frýda and Manda, 2013; Kříž, 1992; Manda and Kříž, 2006; Štorch, 1995; Tonarová et al., 2025; Zhang et al., 2022)(Fig 1C-J). The mid-Ludfordian CIE is subdivided into three chemostratigraphic zones (R, S, and F Zones; Frýda and Manda (2013))(Fig. 1G-J). The R-Zone, marking the rapid positive $\delta^{13}C_{carb}$ shift following the LAD of *P. siluricus*, corresponds to the *P. latialata-O. snajdri* Interval Biozone of Corradini et al. (2015). The S-Zone represents the sustained high $\delta^{13}C_{carb}$ plateau and maximum carbon burial and coincides with the middle part of the *P. latialata-O. snajdri* Interval Biozone. The F-Zone, characterised by a gradual decline in $\delta^{13}C_{carb}$ values, spans the upper part of the *P. latialata-O. snajdri* Interval Biozone and terminates in the *O. crispa* Biozone, reflecting post-extinction recovery and reestablishment of normal marine conditions (Allman et al., 2024; Frýda et al., 2021).

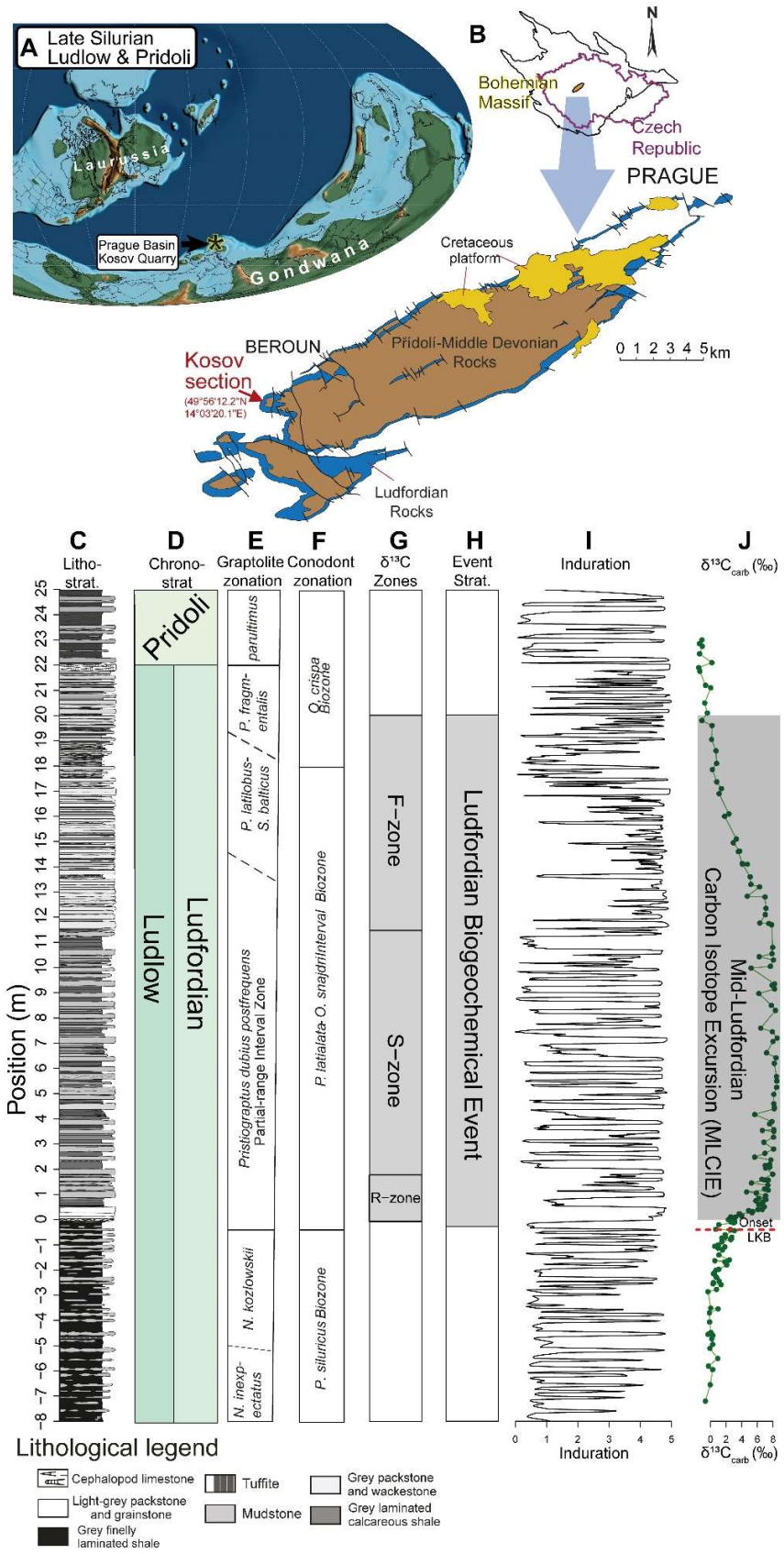
A Late Silurian
Ludlow & Pridoli
Laurussia
Gondwana
Prague Basin
Kosov Quarry
B
N
Bohemian Massif
Czech Republic
PRAGUE
Cretaceous platform
BEROUN
Kosov section
(49°56'12.2"N 14°03'20.1"E)
Pridoli-Middle Devonian Rocks
0 1 2 3 4 5 km
Ludfordian Rocks
C Litho-strat.
D Chrono-strat
E Graptolite zonation
F Conodont zonation
G δ13C Zones
H Event Strat.
I Induration
J δ13Ccarb (‰)
Pridoli
Ludlow
Ludfordian
parultimus
P. fragm-entalis
P. latilobus-S. balticus
Pristiograptus dubius postfrequens Partial-range Interval Zone
N. kozlowskii
N. inexp-ectatus
O. crispa Biozone
P. latialata-O. snajdrilnterval Biozone
P. siluricus Biozone
F-zone
S-zone
R-zone
Ludfordian Biogeochemical Event
Mid-Ludfordian Carbon Isotope Excursion (MLCIE)
Onset LKB
Position (m)
Induration
δ13Ccarb (‰)
Lithological legend
Cephalopod limestone
Light-grey packstone and grainstone
Grey finelly laminated shale
Tuffite
Mudstone
Grey packstone and wackestone
Grey laminated calcareous shale

Fig. 1. Regional overview of the Kosov section. A. Palaeogeography. B. Basinal setting. C. Litholog D. Chronostratigraphy E. Graptolite Zonation F. Conodont Zonation G. Carbon isotope zonation. G. Event stratigraphy. I. Induration record extracted from Fig 1C. J. combined $\delta^{13}C_{carb}$ records of Farkaš et al. (2016) and Frýda et al. (2020) . Noted are the onset of the Lau/Kozlowskii Bioevent and the mid-Ludfordian Carbon Isotope Excursion (MLCIE) after Frýda et al. (2021). A - after Scotese (2021) and Frýda et al. (2021), B-H, J – modified after Frýda and Manda (2013), Frýda et al. (2020) and Frýda et al. (2021).

3. Materials and Methods

A cyclostratigraphic analysis was conducted on the induration record extracted from the litholog published in Frýda et al. (2020) (see https://github.com/stratigraphy/Kosov-cyclostrat for the R code Quarto document). The induration record is considered a proxy for lithification intensity and sedimentary competence, with low values corresponding to soft shales and marl and high values corresponding to competent limestone beds (Frýda et al., 2020; Marsaglia et al., 2017). The cyclostratigraphic study of this induration record used the WaverideR (Arts et al., 2024; Arts, 2023) and Astrochron (Meyers, 2019, 2015) R packages.

The cyclostratigraphic analysis began by applying the Time Optimisation (TimeOpt) function of the astrochron R package to the induration record, yielding a first-order estimate of the sedimentation rate (Meyers, 2015). The TimeOpt function was run twice: once to evaluate the 405-kyr eccentricity amplitude modulation of the 100-kyr eccentricity band and the concentration of power at the 100-kyr and 405-kyr eccentricity frequencies, and once to evaluate the same parameters at the precession and 100-kyr eccentricity

frequencies. The optimal fit of the astronomical cycles was evaluated across a range of sediment accumulation rates from 0.1 to 3 cm/kyr, which encompasses the minimum and maximum estimates of the duration of the studied interval (Arts et al., 2024; Cramer et al., 2015; Melchin et al., 2020).

The first-order sedimentation rate estimate from the TimeOpt runs was used to calculate the period (m) of the 405-kyr eccentricity cycle. Using this information, it was possible to filter the 405-kyr eccentricity cycle from the induration record. The extracted cycle was then used for minimal tuning, in which the distance (m) between successive peaks of the cycle was used to create a period (m) curve for the 405-kyr eccentricity cycle (Hinnov, 2013). This period (m) was then used to guide the tracking of the period (m) of the 405-kyr eccentricity cycle in the CWT scalogram. The tracked period (m) curve was then recalculated using the ratios between the 405-kyr eccentricity cycle and those of other known astronomical cycles. These (recalculated) curves were then overlain on the CWT scalogram to verify whether they passed through regions of high spectral power, thereby validating the presence of known astronomical cycles.

The tracked 405-kyr eccentricity period (m) curve was used to establish an anchored astrochronology by tying the floating timescale to the astrochronologically calibrated age of the Ludlow–Pridoli boundary (423.03 ± 0.53 Ma) (see Arts (2023) for the used technique and see Arts et al. (2024) for the recalibrated age of the Ludlow–Pridoli boundary). The anchored numerical age model was then used to assign ages and durations (with uncertainty) to the record of the Kosov quarry section and its subsections.

The anchored age model also enabled the study of the imprint of astronomical cycles in the induration record in the time domain. Special attention was paid to the phase

relationship between the 100-kyr eccentricity cycle directly extracted from the record and the 100-kyr eccentricity cycle extracted from the Hilbert transform of the precession cycle, and between the 405-kyr eccentricity cycle directly extracted from the record and the 405-kyr eccentricity cycle extracted from the Hilbert transform of the 100-kyr eccentricity cycle. The phase relationship between these cycles allowed inference of the cycle's phases extracted from the proxy record relative to the true phases of the astronomical cycles (Hinnov, 2000; Laskar et al., 2004).

A lag-1 curve was also generated by applying a Monte Carlo simulation of the windowed lag-1 autocorrelation coefficient to the induration record in the time domain. This record functions as a proxy record for the sea-level curve (Li et al., 2018). The imprint of astronomical cycles in the lag-1 record was investigated and compared with that in the induration record to understand the relationship between astronomical forcing and sea-level change during the Ludfordian Biogeochemical Event. The combined $\delta^{13}C_{carb}$ records of Farkaš et al. (2016) and Frýda et al. (2020) were also converted to the time domain, enabling calculation of the rate of change (‰/kyr) on the tuned $\delta^{13}C_{carb}$ record. This record was subsequently investigated for imprint of astronomical cycles.

4. Results

4.1.Building an age model for the Ludfordian Biogeochemical Event

The TimeOpt consistently identifies an optimal sedimentation rate centred at approximately 1.8 cm/ka, with a broader interval of elevated fits between 1.2 and 2.0

275 cm/ka (Fig. 2A, B, E, F). In the TimeOpt run evaluating the 405-kyr eccentricity amplitude
276 modulation of the 100-kyr eccentricity band, together with the concentration of spectral
277 power at the 405-kyr and 100-kyr eccentricity frequencies, both the envelope fit
278 (r^2[envelope]) and the combined optimal fit metric (r^2[opt]) converge toward a pronounced
279 maximum near 1.8 cm/ka. In contrast, the r^2 power spectrum metric displays a less
280 sharply defined response (Fig. 2A, B). At the optimal solution of 1.8cm/kyr, the
281 reconstructed eccentricity model closely tracks the amplitude envelope of the filtered
282 short eccentricity signal, indicating coherent eccentricity-driven amplitude modulation
283 (Fig. 2C, D). In the second TimeOpt run, evaluating the eccentricity amplitude modulation
284 of the precession band and the concentration of power at the precession and 100-kyr
285 eccentricity frequencies, the overall fit of values is lower. Nevertheless, both r^2[envelope]
286 and r^2[opt] again converge toward a maximum at approximately 1.8 cm/kyr, while the r^2
287 power spectrum remains comparatively ambiguous (Fig. 2E, F). At the corresponding
288 optimal solution of 1.8 cm/kyr, the reconstructed eccentricity model follows the amplitude
289 envelope of the filtered precession signal, but with reduced coherence relative to the 405-
290 kyr versus 100-kyr eccentricity modelling run (Fig. 2C, D, G, H).

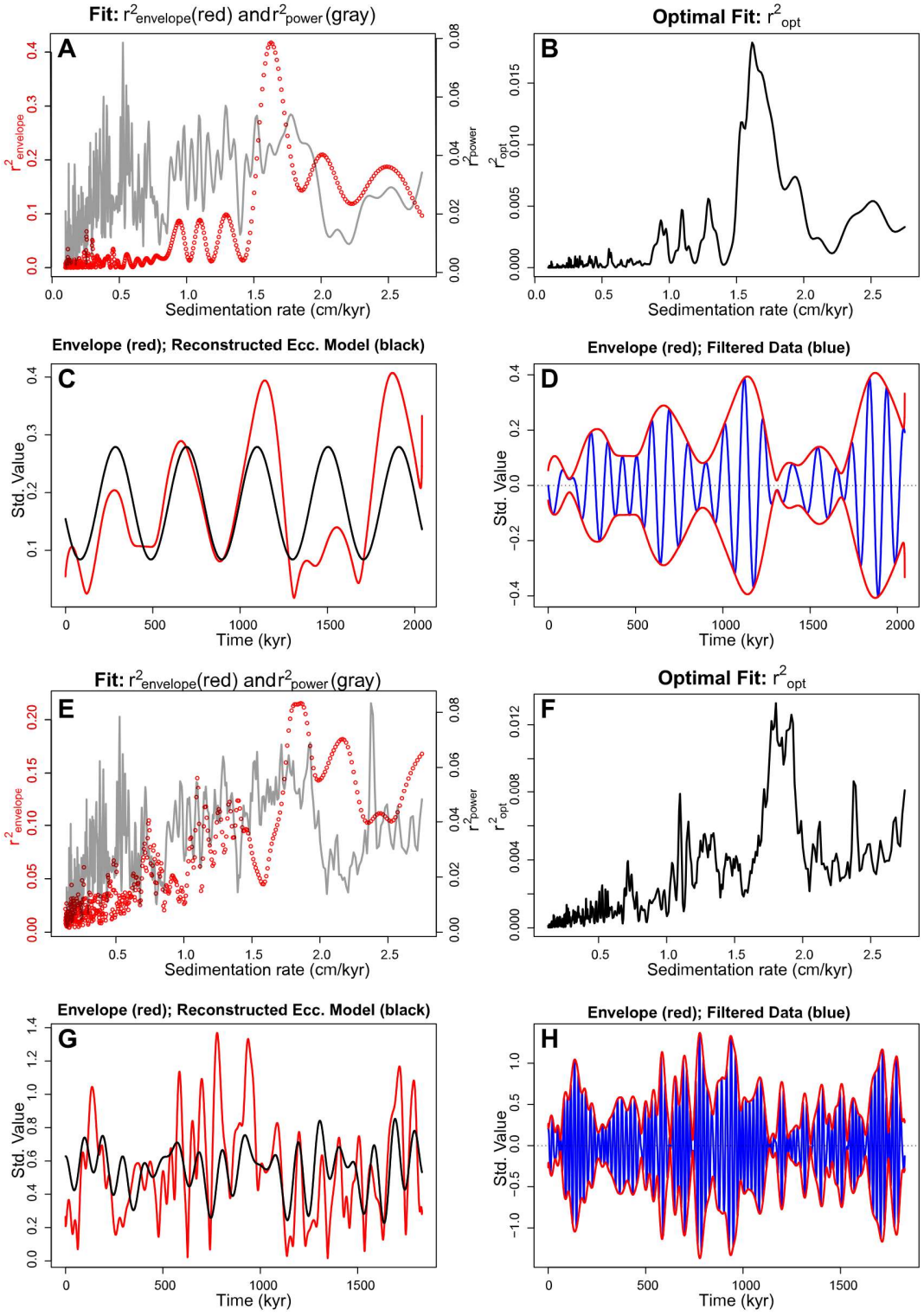
Fit: r2envelope(red) andr2power(gray)
A
r2envelope
r2power
Sedimentation rate (cm/kyr)
Optimal Fit: r2opt
B
r2opt
Sedimentation rate (cm/kyr)
Envelope (red); Reconstructed Ecc. Model (black)
C
Std. Value
Time (kyr)
Envelope (red); Filtered Data (blue)
D
Std. Value
Time (kyr)
Fit: r2envelope(red) andr2power(gray)
E
r2envelope
r2power
Sedimentation rate (cm/kyr)
Optimal Fit: r2opt
F
r2opt
Sedimentation rate (cm/kyr)
Envelope (red); Reconstructed Ecc. Model (black)
G
Std. Value
Time (kyr)
Envelope (red); Filtered Data (blue)
H
Std. Value
Time (kyr)

291

Fig. 2. TimeOpt results. A. Fit: r²[envelope] (red) and r²[power] (grey) for TimeOpt run 405 vs 100-kyr ecc. B. Optimal Fit: r²[opt] for TimeOpt run 405 vs 100-kyr eccentricity. C. Envelope (red); Reconstructed eccentricity. Model (black) for TimeOpt run 405 vs 100-kyr eccentricity. D. Envelope (red); Filtered Data (blue) for TimeOpt run 405 vs 100-kyr eccentricity. E. Fit: r²[envelope] (red) and r²[power] (grey) for TimeOpt run 100-kyr eccentricity versus precession. F. Optimal Fit: r²[opt] for TimeOpt run 100-kyr eccentricity versus precession. G. Envelope (red); Reconstructed eccentricity. Model (black) for TimeOpt run 100-kyr eccentricity versus precession. H. Envelope (red); Filtered Data (blue) for TimeOpt run 100-kyr eccentricity versus precession.

Based on the sedimentation rate estimates obtained from the TimeOpt modelling run, the 405-kyr eccentricity cycle was extracted from the induration record using a Taner band-pass filter spanning 4.86–8.1 m, corresponding to the optimal sedimentation rate range of 1.2–2.0 cm/kyr identified by the TimeOpt modelling run (Figs. 2, 3A). When superimposed on the original signal, the filtered 405-kyr cycle appears as a primary modulating rhythm of intervals with low and high induration values, demonstrating that the cycle is present in the original signal. Not an artefact of signal processing (Fig. 3A). Next, a sedimentation-rate curve was constructed using the minimal-tuning technique, in which the distance between successive peaks of the extracted cycle is set to the duration of the interpreted astronomical cycle (Fig. 3B). This procedure yields a varying sedimentation-rate (cm/kyr) curve (Fig. 3B).

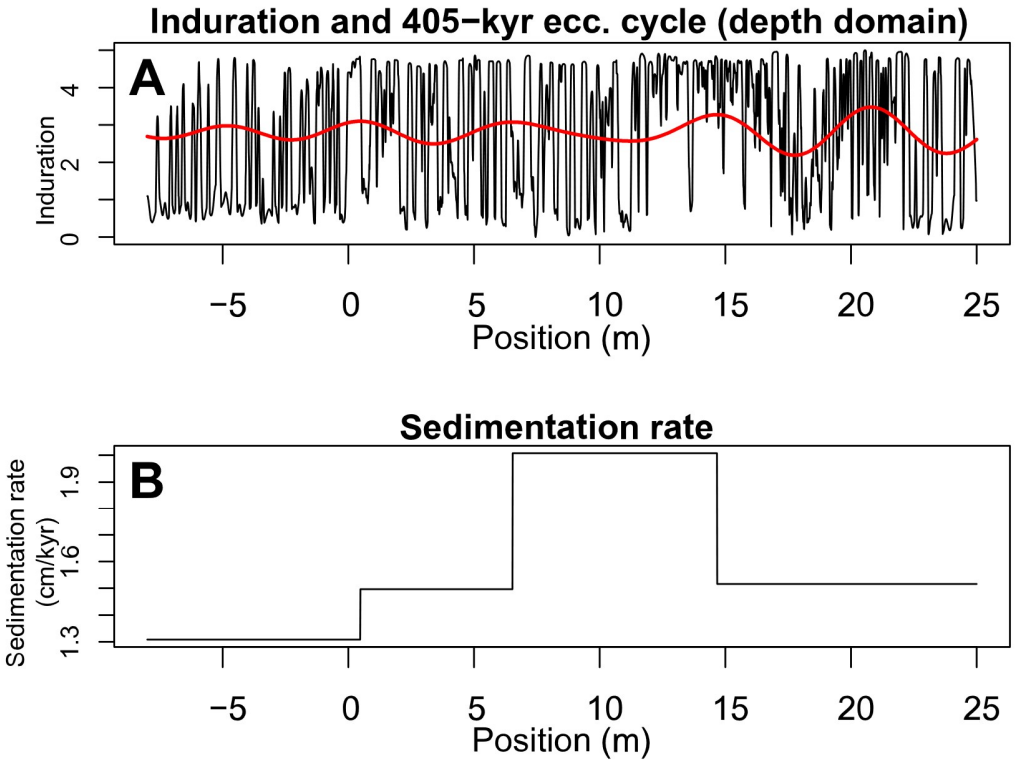

312

313 *Fig. 3. Minimal tuning. A. Induration record and the extracted 405-kyr eccentricity cycle.*

314 *B. Sedimentation rate and sedimentation rate (cm/kyr) based on the minimal tuning.*

315 The sedimentation rate curve (cm/kyr) obtained from the minimal tuning was multiplied

316 by 4.05 to get the corresponding period (m) curve of the 405-kyr eccentricity cycle (Fig.

317 4). This period (m) curve was then superimposed on the continuous wavelet transform

318 (CWT) scalogram (Fig. 4), where the curve can be observed to pass through an area of

319 high spectral power, consistent with the presence of the 405-kyr eccentricity cycle in the

320 induration record. Next, the period (m) of the 405-kyr cycle was tracked within the CWT

321 (shown as the grey line in Fig. 4). To test the validity of this tracked period curve, it was

322 rescaled using the ratios between the 405-kyr eccentricity cycle and the 100-kyr

323 eccentricity, obliquity, and precession cycles (Laskar et al., 2004, 2011; Waltham, 2015).

324 The recalculated period (m) curves for the 100-kyr eccentricity, obliquity, and precession

cycles similarly pass through regions of high spectral power, thereby validating the presence of these cycles and the tracking of the 405-kyr eccentricity cycle in the original CWT.

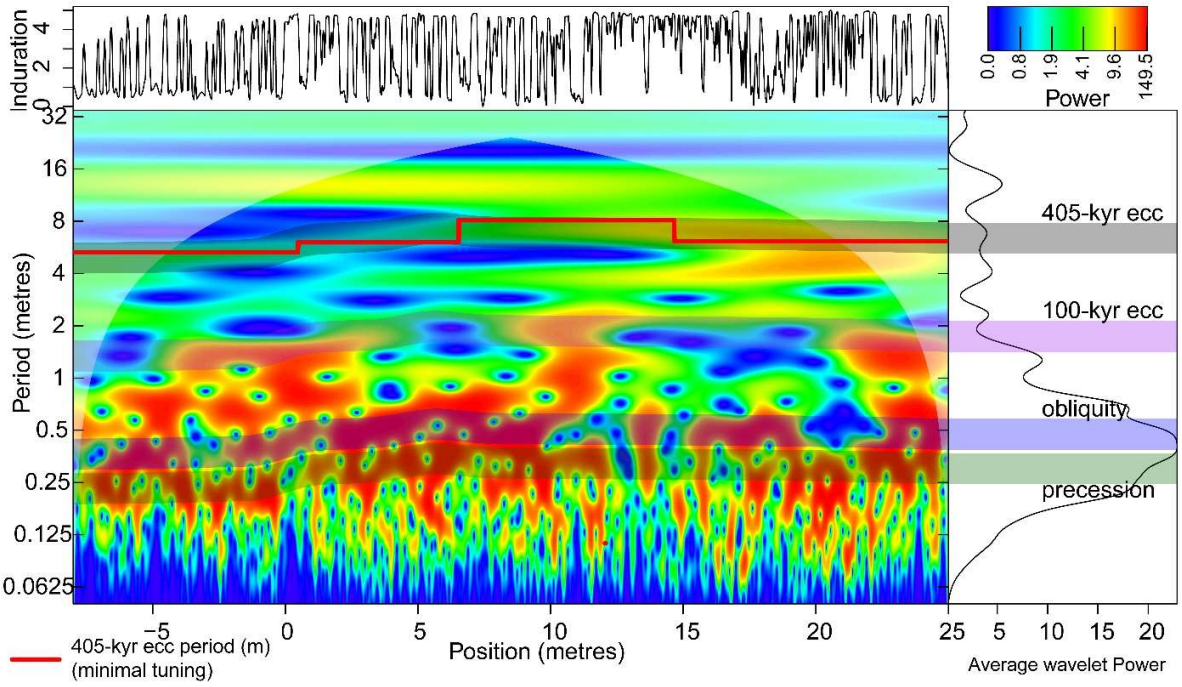

Fig. 4. The Continuous Wavelet Transform (CWT) of the induration record extracted from the litholog of Frýda et al. (2020) and the period (m) of astronomical cycles based on the sedimentation rates attained from the minimal tuning and the tracked period (m) of the 405-kyr eccentricity cycle. Black line = tracked period (m) of the 405-kyr eccentricity cycle. Red line = the period (m) of the 405-kyr eccentricity cycle (minimal tuning based). Purple line = the 100-kyr eccentricity cycle (recalculated tracked period (m) of the 405-kyr eccentricity cycle). Blue line = the obliquity cycle (recalculated tracked period (m) of the 405-kyr eccentricity cycle) Dark green line = the precession cycle (recalculated tracked period (m) of the 405-kyr eccentricity cycle).

The tracked period (m) curve of the 405-kyr eccentricity cycle was used to construct a floating astrochronology, with an assigned uncertainty based on the analytical uncertainty of the wavelet transform (Arts et al., 2024). This floating age model with uncertainty was then anchored to the astrochronologically calibrated age of the Ludlow-Pridoli boundary (423.03 ±0.53 Ma) (Arts et al., 2024) (Fig 5). This anchored numerical age model could then be used to assign ages and durations (with uncertainties) to the records of the Kosov quarry section and its subsections and biozones identified in the succession (Frýda et al., 2021; Frýda and Manda, 2013)(Table 1). The calculated ages, durations, and their associated uncertainties were rounded to the nearest 10 kyr to align with the precision of the anchor point (Table 1).

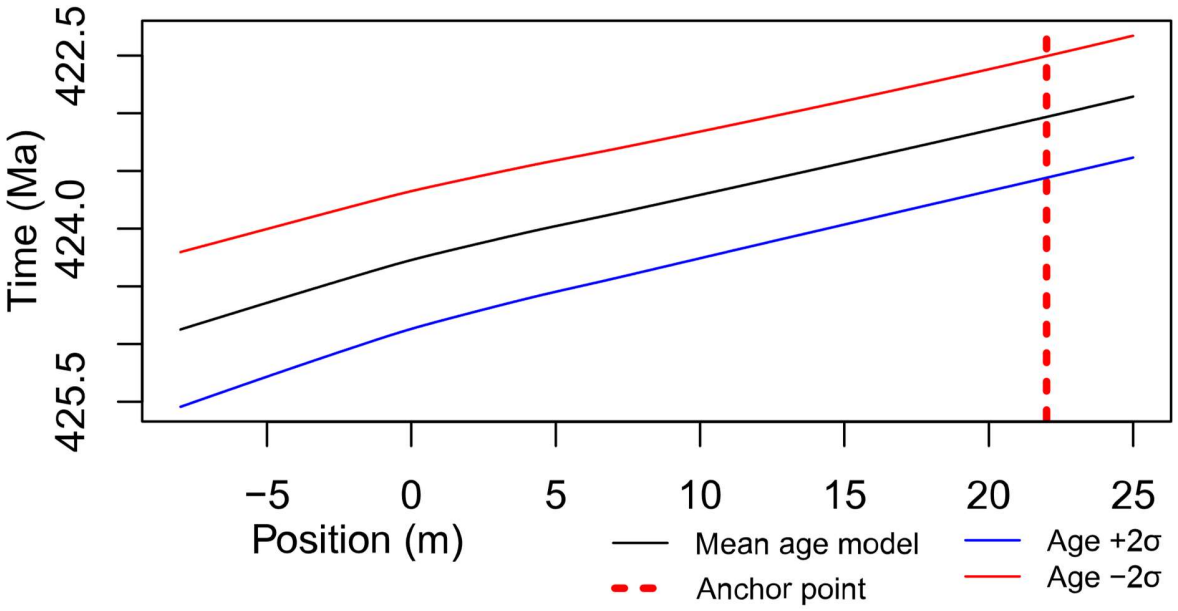

Fig. 5. Astrochronological numerical age- depth model. The black line is the mean age-depth curve, and the red and blue lines are time plus and minus two standard deviations (2σ). The red dotted line is the anchor point at the Ludfordian-Pridoli boundary at 22m.

353 *Table 1. Durations and ages for chronostratigraphic/geochronologic units, lithological*
354 *units, events and conodont zones. All dates are rounded to the nearest 10 kyr to agree*
355 *with the accuracy of the anchor of the Ludfordian-Pridoli boundary.*

Interval	position (m) bottom	position (m) top	Age bottom (Ma) ±2sd	Age top (Ma) ±2sd	duration (kyr) ±2sd
Entire record	-8.00	25.00	424.87 ± 0.67	422.86 ± 0.53	2020 ± 450
Ludfordian Biogeochemical Event	-0.40	20.00	424.30 ± 0.60	423.15 ± 0.53	1150 ± 260
LKB (culmination of the Siluricus ocean Anoxic Event)	-0.40	0.00	424.30 ± 0.60	424.27 ± 0.60	30 ± 10
Mid-Ludfordian Carbon Isotope Excursion (MLCIE)	0.00	20.00	424.27 ± 0.60	423.15 ± 0.53	1120 ± 250
R-zone	0.00	1.40	424.27 ± 0.60	424.18 ± 0.59	90 ± 20
S-Zone	1.40	11.60	424.18 ± 0.59	423.62 ± 0.54	570 ± 130
F-Zone	11.60	20.00	423.62 ± 0.54	423.15 ± 0.53	470 ± 110
Ludlow part section	0.00	22.00	424.27 ± 0.60	423.03 ± 0.53	1240 ± 280
Pridoli part section	22.00	25.00	423.03 ± 0.53	422.86 ± 0.53	180 ± 40
P. siluricus Biozone part section	-8.00	-0.40	424.87 ± 0.67	424.3 ± 0.60	570 ± 130
P. latialata - O. snajdri Interval Biozone	-0.40	18.00	424.3 ± 0.60	423.26 ± 0.53	1040 ± 230
O. crispa Biozone part section	18.00	25.00	423.26 ± 0.53	422.86 ± 0.53	400 ± 90

356 4.2 Proxy records and astronomical cycles in the numerical time
357 domain

358 The age model was used to convert the induration and $\delta^{13}C_{carb}$ records to the numerical
359 time domain (Fig. 6A-E). Subsequently, the continuous wavelet transform (CWT) was
360 applied to the tuned induration record (Fig. 6F). The CWT scalogram reveals distinct

spectral peaks corresponding to astronomical cycles: 8.5-kyr (half precession), ~16-kyr (precession), 28-kyr (obliquity), 50-kyr (eccentricity), 100-kyr (eccentricity), 200-kyr (eccentricity), and 405-kyr (eccentricity) (Fig. 6F). The presence of these spectral peaks in the CWT scalogram validates the underlying age model.

To further analyse these cycles, the precession, obliquity, 100-kyr eccentricity, and 405-kyr eccentricity cycles were extracted from the tuned induration record (Fig. 6F-J). When these extracted cycles are overlaid on the tuned induration record, it becomes evident that obliquity and precession form the fundamental bed-to-bed pattern. The 100-kyr eccentricity cycle also contributes to this pattern. Still, it primarily modulates the rhythm of intervals with low and high induration values, whereas the 405-kyr eccentricity cycle plays a dominant role in modulating the broader stratigraphic trends. Additionally, the Hilbert transform was applied to the precession, obliquity, and 100-kyr eccentricity cycles extracted from the tuned induration record (Fig. 6H, I, K). The 100 and 405-kyr eccentricity cycle was extracted from the Hilbert transform-derived amplitude record of the precession and 100-kyr eccentricity cycle and compared to the 100 kyr and 405-kyr eccentricity cycle directly extracted from the record (Fig. 6H-J). Notably, both the 100-kyr and 405-kyr eccentricity cycles extracted from the Hilbert transform amplitudes of the 100-kyr eccentricity cycle and precession are antiphased relative to their counterparts directly extracted from the induration record (Fig. 6G, J).

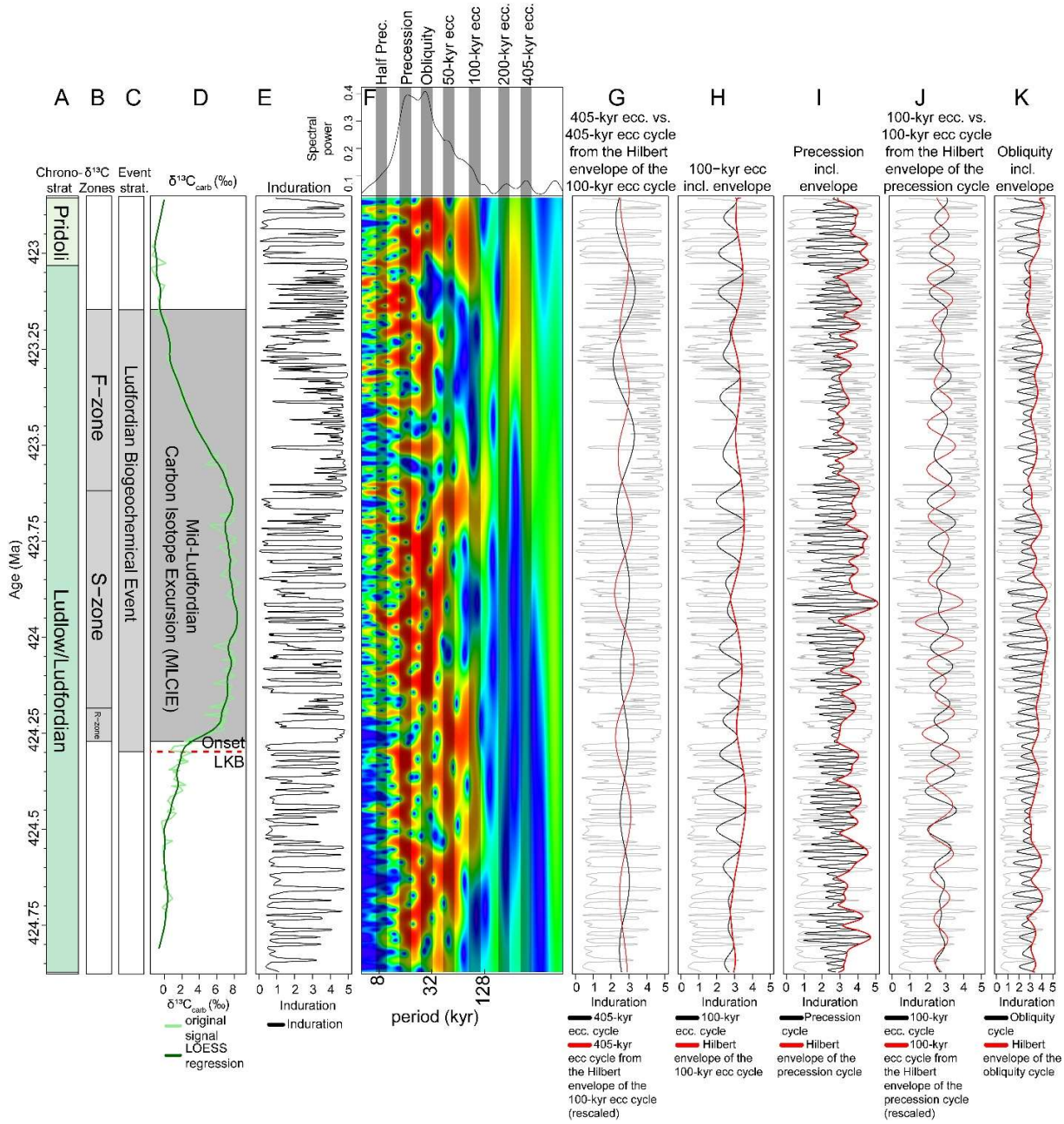

381

382 *Fig. 6. Induration proxy record in the time domain, including the wavelet scalogram of the*
383 *induration record and astronomical cycles extracted from said record. A Stages. B. Event*
384 *zone subdivision C. Event stratigraphy. D. The $\delta^{13}C_{carb}$ record. E. The Induration record.*
385 *F. Wavelet scalogram of the induration record with the average spectral power on top.*
386 *The black vertical lines in the wavelet scalograms are durations of known astronomical*

cycles. From left to right, these cycles are the 8.5-kyr half precession, ~16-kyr precession, 28-kyr obliquity,50-kyr eccentricity, 100-kyr eccentricity, 200-kyr eccentricity and the 405-kyr eccentricity cycle. G. The black line is a 405-kyr eccentricity cycle extracted from the Induration record. The red line is the 405-kyr eccentricity cycle extracted from the Hilbert transform of the 100-kyr eccentricity cycle of the Induration record. H. The 100-kyr eccentricity cycle was extracted from the Induration record (black line) and the Hilbert transform of the 100-kyr eccentricity cycle (red line). I. Precession cycle extracted from the Induration record (black line), and the Hilbert transform of the precession cycle (red line). J. The black line is a 100-kyr eccentricity cycle extracted from the Induration record. The red line is the 100-kyr eccentricity cycle extracted from the Hilbert transform of the precession cycle of the Induration record. K. The obliquity cycle extracted from the Induration record (black line) and the Hilbert transform of the precession cycle (red line).

4.3 The lag-1 sea-level and the $\delta^{13}C_{carb}$ (rate-of-change) curves

The lag-1 autocorrelation coefficient curve (computed with the lag-1 function on WaverideR, via a windowed Monte Carlo analysis, (Fig. 7E) serves as a proxy for sea-level changes (Li et al., 2018). Before the Mid-Ludfordian Carbon Isotope Excursion (MLCIE), the lag-1 sea-level curve is characterised by stable high values, interpreted as high sea-level, superimposed on low-amplitude fluctuations. At the onset of the Lau/Kozlowskii Bioevent (LKB), a minor sea-level rise is observed, followed by a large fall, interpreted as a minor transgression followed by a regression. Afterwards, values stabilise and stay low during the middle of the MLCIE $\delta^{13}C_{carb}$ excursion. At the boundary between the S and F $\delta^{13}C_{carb}$ zones, a large drop is observed, indicative of a regression. Towards the top of the studied succession, the curve returns to higher lag-1 sea-level

values, indicating a major transgression. Prior to the onset of the LBE, no clear imprint of the 100 and 405-kyr eccentricity cycles is detected (Fig. 7E). In contrast, after the onset of the LBE, a moderate imprint of these eccentricity cycles emerges. These signals were extracted and compared with the same cycles extracted from the induration record (Fig. 7F–G). The 100 and 405-kyr eccentricity cycles extracted from the rate lag-1 record are generally anti-phased relative to the eccentricity cycles extracted from the induration record (Fig. 7F–G). The rate of change (‰/kyr) of the $\delta^{13}C_{carb}$ curve was calculated from the LOWESS regression applied to the $\delta^{13}C_{carb}$ record (Fig. 7H-I). The regression was applied to minimise the influence of short-term local noise (Fig. 7H). The rate of change (‰/kyr) reaches a maximum of 0.09 (‰/kyr) during the onset of the LBE (Fig. 7I). The rate-of-change (‰/kyr) record shows a strong imprint of the 100-kyr eccentricity cycle, which was subsequently extracted and plotted alongside the 100-kyr eccentricity cycle from the induration record (Fig. 7I). The 100-kyr eccentricity cycle extracted from the rate-of-change (‰/kyr) record is generally anti-phased with the 100-kyr eccentricity cycle extracted from the induration record (Fig. 7J).

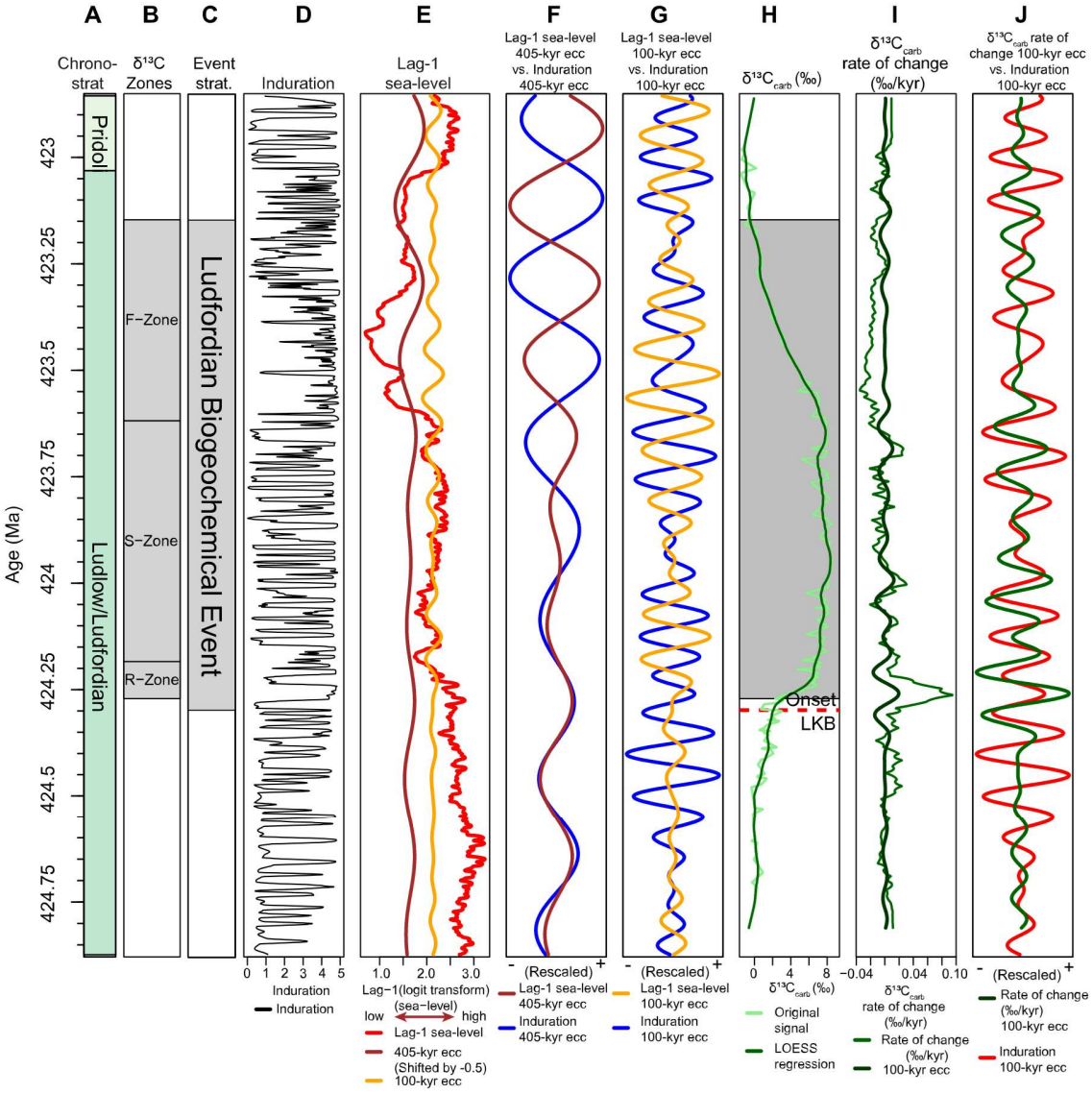

425

426 *Fig. 7. Lag-1 sea-level and rate of change (‰/kyr) of the $\delta^{13}C_{carb}$ record. A Stages. B.*
427 *Event zone subdivision. C. Event stratigraphy. D. The Induration record. E. The lag-1 sea-*
428 *level curve (Logit transform) (red) and the 100 and 405-kyr eccentricity cycle extracted*
429 *from said record (brown) (high values indicate a high sea-level). F. The 405-kyr*
430 *eccentricity cycle extracted from the lag-1 curve (brown) and the 405-kyr eccentricity*
431 *cycle extracted from the Induration record (blue). G. The 100-kyr eccentricity cycle*
432 *extracted from the lag-1 curve (brown) and the 100-kyr eccentricity cycle extracted from*

the Induration record (blue). H. The $\delta^{13}C_{carb}$ record (light green), and the LOWESS smoothed curve (dark green) I. The $\delta^{13}C_{carb}$ rate of change record (‰/kyr) and the 100-kyr eccentricity cycle extracted from said record. J. The 100-kyr eccentricity cycle extracted from the $\delta^{13}C_{carb}$ rate of change record (‰/kyr) (dark green) and the 100-kyr eccentricity cycle extracted from the induration record (red).

5. Discussion

5.1 Astrochronology and the imprint of astronomical cycles through the Ludfordian Biogeochemical Event

The establishment of the astrochronological framework for the Kosov quarry section represents a new step toward quantifying the tempo of the largest carbon isotopic anomaly of the Phanerozoic, the late Silurian Ludfordian Biogeochemical Event (LBE), and towards completing the (Silurian) astronomical timescale. The new anchored astrochronology provides the first virtually complete, high-resolution temporal calibration, allowing us to examine the imprint of astronomical cycles and their role in modulating the processes at play during the LBE.

The anchored astrochronological age model was used to assign ages, durations, and associated uncertainties to chrono- and geochronologic units, lithological units, and events in the Kosov quarry section, as tabulated in Table 1. The LBE started at 424.30 ± 0.60 Ma and lasted 1150 ± 260 kyr. In contrast, the Lau–Kozłowskii Bioevent (LKB) lasted only 30 ± 10 kyr. A previous estimate for the onset of the LBE is based on a dated hiatus in the Cellon section, spanning 424.19 ± 0.55 Ma to 423.83 ± 0.55 Ma (Arts et al., 2024).

Another age constraint is a U–Pb zircon age of 424.08 ± 0.20 Ma, obtained from a bentonite less than one meter below the onset of the positive $\delta^{13}C_{carb}$ excursion (Cramer et al., 2015). The new astrochronologically tuned age for the onset of the LBE (424.30 ± 0.60) falls within the independently derived age range (when accounting for the associated uncertainty), thereby reinforcing the robustness of our results. The estimated uncertainties on event durations are approximately 15%. A future multi-proxy approach on the same interval may further refine the astrochronological framework of the Kosov quarry section (Arts et al., 2024).

By isolating the precession, obliquity, and eccentricity components at 100 and 405-kyr from the tuned induration record (Fig. 6G–K), the hierarchical imprint of astronomical forcing on the Kosov Quarry succession becomes particularly clear. Bed-scale induration alternations are predominantly paced by precession and obliquity. In contrast, their stratigraphic organisation into bundles is controlled by eccentricity, consistent with eccentricity's role in modulating the amplitude of the precession cycle. This observation further supports an astronomically forced origin of the observed induration patterns.

The periods interpreted as obliquity (28 kyr) and precession (16 kyr) cycles are at the shorter end of the typically expected durations for the Silurian (Farhat et al., 2022; Waltham, 2015; Wu et al., 2024), yet remain within the current uncertainty range for the estimated durations of these cycles during the Silurian. A spectral peak of ~55 kyr was observed in the average CWT scalogram (Fig. 6F). This spectral peak could correspond to the 55-kyr or 54-kyr eccentricity cycle or the 52.8-kyr obliquity cycle (Laskar, 2020; Laskar et al., 2004), or could be unrelated to astronomical forcing. The spectral power of the 55-kyr cycle is highly variable, indicating that the 55-kyr cycle might be of a transient

nature unrelated to astronomical forcing. A 200-kyr cycle can also be identified in the record(Fig 6F). Given the strong imprint of the 100-kyr and 405-kyr eccentricity cycles, it is reasonable to interpret the 200-kyr cycle as the seldom observed 200-kyr eccentricity cycle (Hilgen et al., 2020).

5.1.1 Phase relationships

The amplitude modulation of astronomical cycles in the induration record provides a critical insight into the phase relationships between proxy signals and “true astronomical cycles, as well as their connection to insolation changes (Arts et al., 2024; Hinnov, 2000; Laurin et al., 2017; Zeeden et al., 2015). Since amplitude-modulating cycles affect the signal amplitude in a unidirectional manner, the astronomical cycles extracted from amplitude records are in phase with their true astronomical cycles counterparts, regardless of whether the proxy responds positively or negatively to insolation forcing, allowing one to uncover the phase relationship between proxy-derived astronomical cycles, the true astronomical cycles, and insolation variations (Arts et al., 2024; Hinnov, 2000; Laurin et al., 2017; Zeeden et al., 2015)(SI 1). The 100 and 405-kyr eccentricity cycles extracted from the amplitude records of the precession and 100-kyr eccentricity cycles, respectively, show an anti-phase relationship with the corresponding eccentricity cycles directly extracted from the induration record (Fig. 6G, J). This relationship indicates that minima in the astronomical eccentricity, obliquity, and precession cycles correspond to maxima in the equivalent components extracted from the induration record. Consequently, this indicates that peaks in the induration values occur during austral summer insolation minima. A plausible mechanism that can be invoked to explain this insolation to proxy relationship is that during austral summer insolation minima,

seasonality decreased, reducing runoff pulses resulting enhanced carbonate production leading to higher induration values, whereas during austral summer insolation maxima, seasonality increases, resulting in higher runoff, increased detrital products, and decreased carbonate productivity, leading to lower induration values (Martinez, 2018; Mutterlose and Ruffell, 1999).

The established relationship between insolation and induration can also be used to interpret the imprint of astronomical cycles on the rate of change (‰/kyr) of the $\delta^{13}C_{carb}$ record and the lag-1 sea-level curve. Since the 100-kyr eccentricity cycle extracted from the rate of change (‰/kyr) record is generally in phase with the 100-kyr eccentricity cycle extracted from the induration record, it can be inferred that the $\delta^{13}C_{carb}$ rate of change (‰/kyr) is the highest during astronomical eccentricity minima (Fig. 7J). The 100 and 405-kyr eccentricity cycles extracted from the rate lag-1 record are generally antiphased with the 100 and 405-kyr eccentricity cycles extracted from the induration record, indicating that sea level is highest during astronomical eccentricity maxima (Fig. 7F-G).

5.2 Astronomical pacing of the lag-1 sea-level curve

The lag-1 curve used as a proxy for relative sea level at the Kosov quarry section is consistent with previous sea-level reconstructions for the basin, which indicate two major sea-level falls during the LBE (Frýda et al., 2021). The two regressions observed in the lag-1 record (Fig 7E) during the LBE align with widespread sedimentological and isotopic evidence for glacio-eustatic sea-level drawdown associated with the Mid-Ludfordian Glaciation, as reported from Laurentia, Baltica, and Gondwana (Cherns, 1982; Eriksson and Calner, 2008; Frýda et al., 2021; Jeppsson et al., 2007; Kiipli et al., 2010; Lehnert et

522 al., 2007a, 2007b; Manda and Kříž, 2006; Trotter et al., 2016). Together, these
523 observations support the interpretation that a short-lived icehouse episode occurred
524 within an otherwise greenhouse-like late Silurian climate. The lag-1 curve further indicates
525 that the second regression during the LBE was larger than the first. Although this
526 difference has not been explicitly quantified in earlier studies, it is consistent with the
527 stratigraphic record of two distinct karstification surfaces developed across shallow-
528 marine carbonate platforms during this interval (Cherns, 1982; Eriksson and Calner,
529 2008; Frýda et al., 2021; Lehnert et al., 2007a). These surfaces provide independent
530 support for a stepwise intensification of sea-level lowering through the LBE, culminating
531 in the Mid-Ludfordian Glaciation. Indeed, the lag-1 record contains 100 and 405-kyr
532 eccentricity cycles that are generally antiphased with those extracted from the induration
533 record, indicating that sea level was highest during eccentricity maxima (Fig. 7F). This
534 relationship between astronomical forcing and sea level is similar to that observed during
535 a glacio-eustatic regime (Lourens and Hilgen, 1997; Li et al., 2018). The emergence of a
536 clearer eccentricity signal during the LBE suggests that astronomically paced glacio-
537 eustatic fluctuations were amplified by climatic changes associated with the Event,
538 ultimately culminating in the Mid-Ludfordian Glaciation (Frýda et al., 2021).

539 5.3 Evaluating the drivers and pacing of carbon-cycle change
540 during the Ludfordian Biogeochemical Event

541 Quantifying the rate of $\delta^{13}C_{carb}$ change (‰/kyr) provides direct insight into the sensitivity
542 and feedback timescales of the Silurian carbon cycle. Until now, the tempo of major
543 Palaeozoic carbon-isotope excursions has remained largely unconstrained, limiting

544 comparisons with its younger Mesozoic and Cenozoic counterparts. The comparison
545 between $\delta^{13}C_{carb}$excursions is further complicated since changes in $\delta^{13}C_{carb}$ are usually
546 reported over discrete intervals of tens to hundreds of kiloyears, and rarely calculated
547 directly from the $\delta^{13}C_{carb}$ curve; consequently, for most perturbations, we know the overall
548 magnitude and duration from onset to peak, but the true rates of change of the excursion
549 remain unresolved. The new astrochronologically anchored age model presented here
550 enables the first robust estimation of $\delta^{13}C_{carb}$ change rates across the LBE (Fig 7H).

551 During the LBE, the $\delta^{13}C_{carb}$ rate of change reached a maximum of 0.09 ‰ per kyr (Fig.
552 7H). These $\delta^{13}C_{carb}$ rate-of-change values were derived from a LOWESS regression of
553 the $\delta^{13}C_{carb}$ curve to minimise short-term local noise, providing a stable regional and
554 potentially global reference for the LBE. The maximum rate of change of 0.09 (‰/kyr) is
555 four times higher than the ~0.02 ‰ per kyr estimate calculated from the $\delta^{13}C_{carb}$ curve of
556 the GTS 2020 reference (Cramer and Jarvis, 2020) (Fig. 8C, D). Unlike the spline-based
557 age interpolation in GTS 2020, which lacks the resolution to capture rapid changes
558 associated with biogeochemical events, the astronomically calibrated age model provides
559 a continuous timescale that allows for reliable rate-of-change estimates (Gradstein et al.,
560 2020). The higher values reported here may therefore better represent the actual rates of
561 change in $\delta^{13}C_{carb}$. Furthermore, these results highlight the importance of
562 cyclostratigraphic approaches for establishing high-resolution age control, enabling
563 precise characterisation of the tempo and structure of (Silurian) biogeochemical events
564 and their associated carbon-cycle perturbations.

565 Following the same principle as for other proxies, it can be established that the 100-kyr
566 eccentricity cycle exerted a primary control over carbon-cycle dynamics during the LBE

and that the rate of change of the $\delta^{13}C_{carb}$ record (‰/kyr) is generally anti-phased with the 100-kyr eccentricity cycle and is the highest during astronomical eccentricity minima (Figs. 7H-J and 8D). The observed phase relationship aligns with a scenario in which eccentricity minima decrease the amplitude of climatic precession, thereby reducing seasonality and creating more stable conditions that favoured the burial and preservation of carbon in quasi-stable carbon reservoirs (Laurin et al., 2017, Laurin et al., 2015; Sproson, 2020; Sproson et al., 2022). The eccentricity-paced fluctuations in carbon storage and release likely contributed to transient atmospheric CO_2 drawdown and cooling, facilitating glacial expansion during the LBE (Frýda et al., 2021; Sproson et al., 2022).

Although astronomical forcing provides a compelling explanation for the pacing of $\delta^{13}C_{carb}$ change, the marked amplification of change-rate amplitudes during the LBE indicates that it alone is insufficient to account for the full magnitude of the response (Fig. 7H). The Silurian P-S climate state model provides a mechanism for amplifying the carbon-cycle response (Bickert et al., 1997; Calner, 2008; Cramer and Saltzman, 2005; Jeppsson, 1990; Jeppsson et al., 1995). This model describes a shift between two distinct climate states: the P-state, characterised by low-latitude humid conditions, enhanced continental runoff, and marl-dominated sedimentation, and the S-state, marked by low-latitude aridity, reduced runoff, and increased carbonate production and reef growth. The transition from P- to S-state would have reduced low-latitude freshwater input, activated low-latitude downwelling centres, reorganised ocean circulation, and intensified water-column stratification, thereby promoting the expansion of deep-ocean anoxia. The resulting quasi-stable carbon reservoirs could have enhanced organic carbon burial, thereby increasing

590 the carbon cycle's sensitivity to astronomical forcing (Sproson, 2020; Sproson et al.,
591 2022). Within this framework, astronomically paced climate variability was more efficiently
592 translated into amplified $\delta^{13}C$ excursions, with astronomical forcing acting as a
593 pacemaker and P–S state transitions amplifying the carbon cycle response.

594 The plausibility of a (P-S) climatic state transition amplification pathway has some merit
595 when considered alongside recent Earth system modelling. Simulations by Pohl et al.
596 (2021, 2022) demonstrate that continental configuration can strongly influence ocean
597 circulation, leading to nonlinear expansions of deep-ocean anoxia under modest climatic
598 forcing. Specifically, Hirnantian simulations show that declining atmospheric pCO_2 and
599 glacio-eustatic sea-level fall promoted widespread deep-water deoxygenation,
600 comparable to the LBE, with rising $\delta^{13}C_{carb}$ values and sea-level fall. Whether low- or high-
601 latitude processes dominated the expansion of Silurian deep-water anoxia remains
602 unresolved and requires further modelling and chemostratigraphic data. The LBE exhibits
603 several features consistent with a P-to-S state switch (Calner, 2005; Crampton et al.,
604 2016; Jeppsson, 1998; Jeppsson and Aldridge, 2000). Yet its similarity to the Hirnantian
605 as modelled by Pohl et al. (2021) suggests that Silurian events may need to be
606 reconsidered within a broader framework of pCO_2 sensitivity and circulation-mode
607 switching. Indeed, the Hirnantian may represent the earliest expression of the circulation
608 instabilities that continued to shape Silurian oceanography, suggesting that later Silurian
609 events were either repeated manifestations of the same underlying paleoceanographic
610 and climatic sensitivities or evolving manifestations of them.

611 Concepts such as circulation-mode switching, pCO_2 sensitivity, and the development of
612 quasi-stable carbon reservoirs are not unique to the Silurian but represent fundamental

613 Earth-system behaviours that can be organised and paced by astronomical cycles
614 (Vervoort et al., 2024; Vervoort et al., 2026; Devleeschouwer 2020, 2020; Laurin et al.,
615 2017; Duplessy and Shackleton, 1985). Placing the LBE within this broader Phanerozoic
616 framework is essential, as it allows Silurian carbon-cycle dynamics to be evaluated
617 alongside younger intervals for which astronomical forcing is firmly established as a
618 primary pacemaker of the climate and carbon cycle (Batenburg et al., 2016; Fang et al.,
619 2025; Laurin et al., 2017; Martinez et al., 2023; De Vleeschouwer, 2020; Westerhold,
620 2020; Zhao et al., 2025). Viewed from this cross-era perspective, the Silurian record
621 provides a critical deep-time test of whether the same astronomically driven mechanisms
622 and feedback structures that shaped known pre-Silurian carbon-cycle perturbations were
623 already operating during the Silurian. While Silurian-specific climatic models have been
624 valuable in linking carbon-cycle perturbations to the geological record, this work
625 demonstrates that integrating concepts such as inclusion of astronomically forced “quasi-
626 stable reservoirs,” a concept originally developed for the Cretaceous and only later
627 hypothesised for the Silurian (Laurin et al., 2017; Sproson et al., 2020), illustrates the
628 value of looking beyond era-specific concepts. By the same logic, but applied in reverse,
629 Silurian-style climate-state transitions and tipping points in the global climate–ocean
630 circulation system may account for apparent discrepancies between the geological record
631 and reconstructed carbon-cycle responses during non-Silurian perturbations, where
632 comparable nonlinear feedback scenarios may have operated but remain unrecognised.
633 The introduction of the novel $\delta^{13}C_{carb}$ rate-of-change curve/proxy further supports this
634 cross-era approach. Comparing the rates calculated in this study with those from
635 GTS2020 already suggests that current non-cyclostratigraphic age models may

significantly underestimate the tempo of Silurian carbon-cycle perturbations (see Fig. 8). This discrepancy underscores the essential role that astrochronologically anchored frameworks play in determining the true rate of change of any Phanerozoic carbon-cycle perturbations. Additionally, the identification of the 100-kyr eccentricity cycle as the primary pacemaker of the Silurian carbon cycle, as evidenced by the $\delta^{13}C_{carb}$ rate-of-change records, demonstrates the utility of this novel proxy for investigating carbon-cycle perturbations. In this context, the LBE serves as a deep-time benchmark for assessing the sensitivity of the Phanerozoic carbon cycle to astronomical forcing and as a template for quantifying the pacing and tempo of carbon-cycle perturbations. Taken together, the astrochronological framework established here demonstrates that the LBE occurred within a highly sensitive Silurian Earth system in which astronomical forcing, carbon burial, sea-level variability, and oceanographic reorganisation were tightly coupled, highlighting the pronounced sensitivity of the early Palaeozoic climate system and carbon cycle to astronomical forcing.

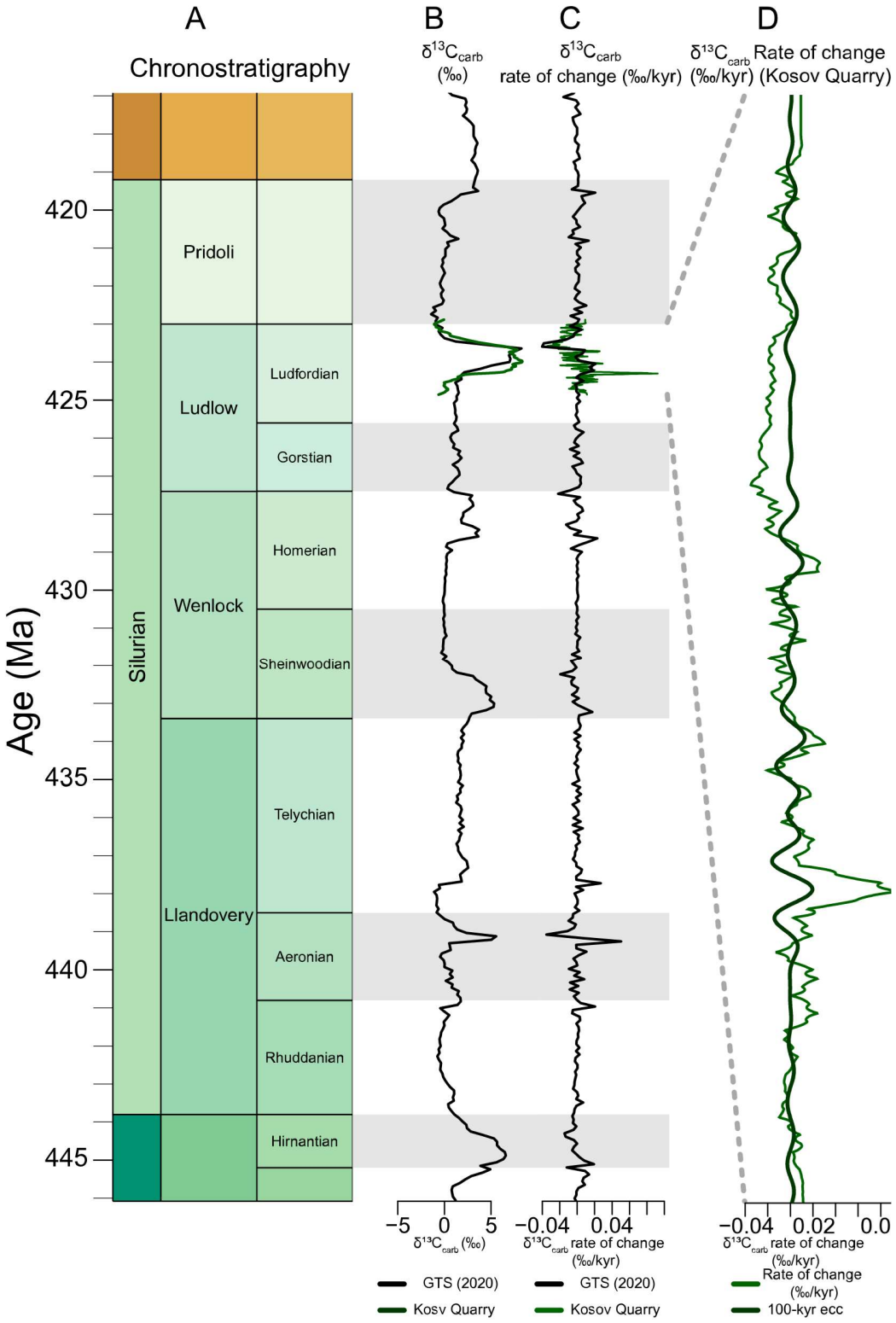
A
Chronostratigraphy
B
δ13Ccarb (‰)
C
δ13Ccarb rate of change (‰/kyr)
D
δ13Ccarb Rate of change (‰/kyr) (Kosov Quarry)
Age (Ma)
420
425
430
435
440
445
Silurian
Pridoli
Ludlow
Wenlock
Llandovery
Ludfordian
Gorstian
Homerian
Sheinwoodian
Telychian
Aeronian
Rhuddanian
Hirnantian
−5 0 5
δ13Ccarb (‰)
−0.04 0.04
δ13Ccarb rate of change (‰/kyr)
−0.04 0.02 0.0
δ13Ccarb rate of change (‰/kyr)
GTS (2020)
Kosv Quarry
GTS (2020)
Kosov Quarry
Rate of change (‰/kyr)
100-kyr ecc

650

Fig. 8. The GTS 2020 its $\delta^{13}C_{carb}$ curve and the $\delta^{13}C_{carb}$ rate of change curve calculated from the $\delta^{13}C_{carb}$ curve, which is compared to the $\delta^{13}C_{carb}$ record and $\delta^{13}C_{carb}$ rate of change record from the Kosov Quarry section. A. Silurian timescale GTS 2020 (shifted up by 0.25 Myrs). B. Silurian $\delta^{13}C_{carb}$ curve from the GTS 2020 (shifted up by 0.25 Myrs) overlain by the $\delta^{13}C_{carb}$ curve of the Kosov Quarry section. C. Silurian $\delta^{13}C_{carb}$ rate of change (‰/kyr) curve calculated based on the $\delta^{13}C_{carb}$ curve from the GTS 2020 (shifted up by 0.4 Myrs) overlain by the $\delta^{13}C_{carb}$ rate of change (‰/kyr) curve based on the one of the Kosov Quarry section. D. The $\delta^{13}C_{carb}$ rate of change record (‰/kyr) and the 100-kyr eccentricity cycle extracted from said record.

6. Conclusions

The new astrochronology from the Kosov Quarry provides the first continuous, anchored astrochronological framework for the Ludfordian Biogeochemical Event (LBE), encompassing the largest positive $\delta^{13}C_{carb}$ excursion of the Phanerozoic. The anchored cyclostratigraphic framework indicates that the LBE began at 424.30 ± 0.62 Ma and lasted 1150 ± 260 kyr, whereas the associated Lau–Kozłowskii Bioevent was considerably shorter, spanning only about 30 ± 10 kyr. Using the cyclostratigraphic framework, we calculated that the $\delta^{13}C_{carb}$ rate-of-change reached a maximum of 0.09 ‰/kyr) during the onset of the LBE. Multiple proxy records show a pervasive imprint of astronomical cycles, with cycles ranging from the 8.5-kyr half-precession to the 405-kyr eccentricity cycle. Phase relationships inferred from the amplitude modulation of lower-order cycles by higher-order astronomical cycles indicate that the induration record is antiphased, with low induration corresponding to austral summer insolation minima, consistent with a

673 scenario in which reduced runoff enhanced carbonate production. This phase relationship
674 study was also extended to the lag-1 sea-level curve and $\delta^{13}C_{carb}$ rate-of-change curve.
675 This shows that the 100 and 405-kyr eccentricity cycles extracted from the lag-1 sea-level
676 curve are in phase with astronomical eccentricity maxima, indicating astronomically
677 paced glacio-eustatic fluctuations consistent with a short-lived icehouse phase in the late
678 Silurian. Critically, the $\delta^{13}C_{carb}$ rate-of-change curve contains a strong 100-kyr eccentricity
679 signal that is antiphased with astronomical eccentricity, providing the first direct evidence
680 that eccentricity paced the carbon cycle during the Silurian. This also represents the first
681 documentation of eccentricity-paced $\delta^{13}C$ rate changes, establishing the $\delta^{13}C_{carb}$ rate-of-
682 change curve as a novel and powerful proxy for investigating carbon-cycle perturbations
683 across the Phanerozoic. While astronomical forcing robustly accounts for the observed
684 pacing, the increase in amplitude of the carbon-cycle's response during the LBE required
685 an additional amplification mechanism. This was likely driven by the characteristic Silurian
686 transition between (P- and S) climatic states, during which shifts in oceanographic
687 circulation and redox architecture created a quasi-stable deep-ocean reservoir.
688 Collectively, these findings establish the LBE as a cornerstone for evaluating the
689 sensitivity of the early Palaeozoic carbon cycle to astronomical forcing, with implications
690 for understanding the tempo and feedback structure of Phanerozoic Earth-system change
691 more broadly.

692

CRediT authorship contribution statement

Michiel Arts: Conceptualisation, Data curation, Formal Analysis, Investigation, Methodology, Project administration, Resources, Software, Validation, Visualisation, Writing–original draft, Writing–review and editing. **Damien Pas**: Writing–review and editing. **Jiří Frýda**: Writing–review and editing. **Anne-Christine da Silva:** Funding acquisition, Supervision, Writing–review and editing.

Declaration of competing interest

The authors declare that they have no known competing financial interests or personal relationships that could have appeared to influence the work reported in this paper.

Declaration of generative AI and AI-assisted technologies in the manuscript preparation process

During the preparation of this work, the author(s) used OpenAI ChatGPT, Mistral AI, and Google Gemini with language editing, text restructuring, and basic coding tasks. After using this tool/service, the author(s) reviewed and edited the content needed and take(s) full responsibility for the content of the published article.

Acknowledgements

The FNRS-PDR T.0051.19 grant supported MA. DP. acknowledges the Swiss National Science Foundation grant PZ00P2-193520. JF. was supported by the Grant Agency of the Czech Republic (project GA23-06198S to JF.)

Data availability statement

The data and materials supporting the findings of this study are presented in the article and its supplementary materials. The R code, Quarto document, generated HTML file with embedded R code, and all associated datasets and results are publicly available at https://github.com/stratigraphy/Kosov-cyclostrat and or https://zenodo.org/records/18165299/files/curve2time_unc_anchor_res.rds. Further inquiries may be directed to the corresponding author.

References

Aldridge, R.J., Jeppsson, L., Dorning, K.J., 1993. Early Silurian oceanic episodes and events. Journal - Geological Society (London) 150, 501–513. https://doi.org/10.1144/gsjgs.150.3.0501

Allman, L.J., Bowman, C.N., Frýda, J., Kozik, N.P., Owens, J.D., Young, S.A., 2024. Constraining reducing conditions in the Prague Basin during the late Silurian Lau/Kozlowskii extinction event. Journal of the Geological Society 181. https://doi.org/10.1144/jgs2023-108

727 Arts, M., 2023. WaverideR: Extracting Signals from Wavelet Spectra. https://cran.r-
728 project.org/web/packages/WaverideR/index

729 Arts, M., Corradini, C., Pondrelli, M., Pas, D., Da Silva, A.C., 2024. Age and astronomical
730 forcing in the upper Silurian Cellon section (Carnic Alps, Austria) uncovered using the
731 WaverideR R package. Frontiers in Earth Science 12, 1–24.
732 https://doi.org/10.3389/feart.2024.1357751

733 Batenburg, S.J., De Vleeschouwer, D., Sprovieri, M., Hilgen, F.J., Gale, A.S., Singer,
734 B.S., Koeberl, C., Coccioni, R., Claeys, P. and Montanari, A., 2016. Astronomical control
735 on the timing of oceanic anoxia in the Late Cretaceous. Climate of the Past, 12(10),
736 pp.1995-2009.Becker, T.R., Marshall, J.E.A., Da Silva, A.C., Agterberg, F.P., Gradstein,
737 F.M., Ogg, J.G., 2020. The Devonian Period, Geologic Time Scale 2020. BV.
738 https://doi.org/10.1016/B978-0-12-824360-2.00022-X

739 Berner, R.A., 2004. The phanerozoic carbon cycle: CO2 and O2. Oxford University Press.
740 https://doi.org/10.1093/oso/9780195173338.001.0001

741 Bickert, T., Pätzold, J., Samtleben, C., Munnecke, A., 1997. Paleoenvironmental changes
742 in the Silurian indicated by stable isotopes in brachiopod shells from Gotland, Sweden.
743 Geochimica et Cosmochimica Acta 61, 2717–2730. https://doi.org/10.1016/S0016-
744 7037(97)00136-1

745 Calner, M., 2005. A Late Silurian extinction event and anachronistic period. Geology 33,
746 305–308. https://doi.org/10.1130/G21185.1

747 Calner, M., Eriksson, M.J., 2006. Evidence for rapid environmental changes in low
748 latitudes during the Late Silurian Lau Event: The Burgen-1 drillcore, Gotland, Sweden.
749 Geological Magazine 143, 15–24. https://doi.org/10.1017/S001675680500169X

750 Calner, M., 2008. Silurian global events - At the tipping point of climate change. Mass
751 Extinction 21–57. https://doi.org/10.1007/978-3-540-75916-4_4

752 Calvert, S., Pedersen, T., 1992. Organic carbon accumulation and preservation in marine
753 sediments: How important is anoxia? pp. 231–263. https://doi.org/10.1111/j.1365-
754 3091.1982.tb00086.x

755 Cherns, L., 1982. Palaeokarst, tidal erosion surfaces and stromatolites in the Silurian Eke
756 Formation of Gotland, Sweden. Sedimentology, 29(6), pp.819-833.

757 Claussen, A.L., 2024. Benthic response to the strong Silurian climatic fluctuations-
758 implications from Gotland (Sweden). Facies. 70, 14 https://doi.org/10.1007/s10347-024-
759 00686-x

760 Cramer, B.D., Jarvis, I., 2020. Chapter 11 - Carbon Isotope Stratigraphy, in: Carbon
761 Isotope Stratigraphy. Elsevier B.V. https://doi.org/10.1016/B978-0-12-824360-2.00011-5

762 Cramer, B.D., Saltzman, M.R., 2007b. Early Silurian paired δ13Ccarb and δ13Corg
763 analyses from the Midcontinent of North America: Implications for paleoceanography and
764 paleoclimate. Palaeogeography, Palaeoclimatology, Palaeoecology 256, 195–203.
765 https://doi.org/10.1016/j.palaeo.2007.02.032

766 Cramer, B.D., Saltzman, M.R., 2007a. Fluctuations in epeiric sea carbonate production
767 during Silurian positive carbon isotope excursions: A review of proposed

768 paleoceanographic models. Palaeogeography, Palaeoclimatology, Palaeoecology 245,
769 37–45. https://doi.org/10.1016/j.palaeo.2006.02.027

770 Cramer, B.D., Saltzman, M.R., 2005. Sequestration of 12C in the deep ocean during the
771 early Wenlock (Silurian) positive carbon isotope excursion. Palaeogeography,
772 Palaeoclimatology, Palaeoecology 219, 333–349.
773 https://doi.org/10.1016/j.palaeo.2005.01.009

774 Cramer, B.D., Schmitz, M.D., Huff, W.D., Bergström, S.M., 2015. High-precision u–pb
775 zircon age constraints on the duration of rapid biogeochemical events during the ludlow
776 epoch (Silurian period). Journal of the Geological Society 172, 157–160.
777 https://doi.org/10.1144/jgs2014-094

778 Crampton, J.S., Cooper, R.A., Sadler, P.M., Foote, M., 2016. Greenhouse−icehouse
779 transition in the Late Ordovician marks a step change in extinction regime in the marine
780 plankton. Proceedings of the National Academy of Sciences of the United States of
781 America 113, 1498–1503. https://doi.org/10.1073/pnas.1519092113

782 del Rey, Á., Frýda, J., Calner, M., Frýdová, B., Zhang, F., Wang, Ch., Planavsky, N., Dahl,
783 T.W., 2023. Mid-Ludfordian uranium isotope records distinguish the role of expansive
784 marine anoxia in global carbon cycle dynamics during the late Silurian Lau/Kozlowskii
785 bioevent. Planetary and Global Change, 229, 1-9.
786 https://doi.org/10.1016/j.gloplacha.2023.104248.

787 De Vleeschouwer, D., Drury, A.J., Vahlenkamp, M., Rochholz, F., Liebrand, D., Pälike,
788 H., 2020. High-latitude biomes and rock weathering mediate climate–carbon cycle

789 feedbacks on eccentricity timescales. Nature Communications 11, 5013.
790 https://doi.org/10.1038/s41467-020-18733-w

791 De Vleeschouwer, D., Percival, L.M.E., Wichern, N.M.A., Batenburg, S.J., 2024. Pre-
792 Cenozoic cyclostratigraphy and palaeoclimate responses to astronomical forcing. Nature
793 Reviews Earth and Environment 5, 59–74. https://doi.org/10.1038/s43017-023-00505-x

794 Duplessy, J.C, Shackleton, N.J., 1985. Response of global deep-water circulation to
795 Earth's climatic change 135,000–107,000 years ago. *Nature*, *316*(6028), pp.500-507.

796 Emeis, K.C., Weissert, H., 2009. Tethyan-Mediterranean organic carbon-rich sediments
797 from Mesozoic black shales to sapropels. Sedimentology 56, 247–266.
798 https://doi.org/10.1111/j.1365-3091.2008.01026.x

799 Eriksson, M.J., Calner, M., 2008. A sequence stratigraphical model for the Late
800 Ludfordian (Silurian) of Gotland, Sweden: Implications for timing between changes in sea
801 level, palaeoecology, and the global carbon cycle. Facies 54, 253–276.
802 https://doi.org/10.1007/s10347-007-0128-y

803 Fang, Q., Wu, H., Montañez, I.P., Shen, S.Z., Zeeden, C., Wang, X., Zhang, S. and De
804 Vleeschouwer, D., 2025. Synchronizing climate-carbon cycle heartbeats in the
805 Phanerozoic vegetated icehouses. Nature Communications, 16(1), p.9196.

806 Farkaš, J., Frýda, J. , Holmden, C., 2016. Calcium isotope constraints on the marine
807 carbon cycle and CaCO3 deposition during the late Silurian (Ludfordian) positive $\delta^{13}C$
808 excursion. Earth and Planetary Science Letters 451, 31–40. DOI
809 10.1016/j.epsl.2016.06.038

Farkaš. J., Wallmann, K., Mosley, L., Staudigel, P., Zheng, X.-Y., Leyden, E., Shao, Y., Frýda, J., Holmden, C. , Eisenhauer, A. 2024. Alkalinity and elemental cycles in present and past ocean: Insight from Geochemical Modeling and Alkali and Alkaline Earth Metal Isotopes, 33–87. In Reference Module in Earth Systems and Environmental Sciences. Treatise on Geochemistry 5. Elsevier, Rotterdam. https://doi.org/10.1016/B9780323997621.000371b

Farhat, M., Auclair-Desrotour, P., Boué, G., Laskar, J., 2022. The resonant tidal evolution of the Earth-Moon distance. Astronomy & Astrophysics 665, L1. https://doi.org/10.1051/0004-6361/202243445

Fatka, O., Mergl, M., 2009. The “microcontinent” Perunica: Status and story 15 years after conception. Geological Society, London, Special Publications 325, 65–101. https://doi.org/10.1144/SP325.4

Frýda, J., Lehnert, O., Frýdová, B., Farkaš, J., Kubajko, M., 2020. Carbon and sulfur cycling during the mid-Ludfordian anomaly and the linkage with the late Silurian Lau/Kozlowskii Bioevent. Palaeogeography, Palaeoclimatology, Palaeoecology 564, 110152. https://doi.org/10.1016/j.palaeo.2020.110152

Frýda, J., Lehnert, O., Joachimski, M.M., Männik, P., Kubajko, M., Mergl, M., Farkaš, J., Frýdová, B., 2021. The Mid-Ludfordian (late Silurian) Glaciation: A link with global changes in ocean chemistry and ecosystem overturns. Earth-Science Reviews 220, 103652. https://doi.org/10.1016/j.earscirev.2021.103652

Frýda, J., Manda, Š., 2013. A long-lasting steady period of isotopically heavy carbon in the late Silurian ocean: Evolution of the delta;13 record and its significance for an

832 integrated delta;13, graptolite and conodont stratigraphy. Bulletin of Geosciences 463–
833 482. https://doi.org/10.3140/bull.geosci.1436

834 Gambacorta, G., Bersezio, R., Weissert, H., Erba, E., 2016. Onset and demise of
835 Cretaceous oceanic anoxic events: The coupling of surface and bottom oceanic
836 processes in two pelagic basins of the western Tethys. Paleoceanography 31, 732–757.
837 https://doi.org/10.1002/2015PA002922

838 Gradstein, F. M., Ogg, J. G., Schmitz, M. D. , Ogg, G. M. 2020. Chapter 14 -
839 geomathematics. in Geologic time scale 2020 (eds) 401–439.
840 https://doi.org/10.1016/B978-0-12-824360-2.00014-0.

841 Gregory, J.M., Jones, C.D., Cadule, P., Friedlingstein, P., 2009. Quantifying carbon cycle
842 feedbacks. Journal of Climate 22, 5232–5250. https://doi.org/10.1175/2009JCLI2949.1

843 Hays, J.D.D., Imbrie, J.Z., Shackleton, N.J., 1976. Variations in the earth's orbit:
844 Pacemaker of the ice ages. Science 194, 1121–1132.
845 https://doi.org/10.1126/science.194.4270.1121

846 Hilgen, F., Zeeden, C., Laskar, J., 2020. Paleoclimate records reveal elusive 200-kyr
847 eccentricity cycle for the first time. Global and Planetary Change 194, 103296.
848 https://doi.org/10.1016/j.gloplacha.2020.103296

849 Hinnov, L.A., Hilgen, F.J., 2012. Cyclostratigraphy and astrochronology. The geologic
850 time scale 2012, 63–83. https://doi.org/10.1016/B978-0-444-59425-9.00004-4

851 Hinnov, L.A., 2000. New Perspectives on Astronomically Forced Stratigraphy. Annual
852 Review of Earth and Planetary Sciences 28, 419–475.
853 https://doi.org/10.1177/0741713604268894

854 Hinnov, L.A., 2013. Cyclostratigraphy and its revolutionizing applications in the earth and
855 planetary sciences. Bulletin of the Geological Society of America 125, 1703–1734.
856 https://doi.org/10.1130/B30934.1

857 Hinnov, L.A., 2018. Cyclostratigraphy and Astrochronology in 2018, Stratigraphy &
858 Timescales. Elsevier Ltd. https://doi.org/10.1016/bs.sats.2018.08.004

859 Horný, R., 1955. Base vrstev kopaninských eß 1 na jihozápadním okraji vulkanické facie
860 (Kosov u Berouna). Věstník Ústředního ústavu geologického 30, 81–86.

861 Huang, H., Gao, Y., Ma, C., Jones, M.M., Zeeden, C., Ibarra, D.E., Wu, H., Wang, C.,
862 2021. Organic carbon burial is paced by a ~173-ka obliquity cycle in the middle to high
863 latitudes. Science Advances 7, 1–11. https://doi.org/10.1126/sciadv.abf9489

864 Isson, T.T., Planavsky, N.J., Coogan, L.A., Stewart, E.M., Ague, Jay.J., Bolton, E.W.,
865 Zhang, S., McKenzie, N.R., Kump, L.R., 2020. Evolution of the global carbon cycle and
866 climate regulation on earth. Global Biogeochemical Cycles 34.
867 https://doi.org/10.1029/2018GB006061

868 Jeppsson, L., 1998. Silurian oceanic events. Summary of general characteristics, in: New
869 York State Museum Bulletin. pp. 239–257.

870 Jeppsson, L., 1990. An oceanic model for lithological and faunal changes tested on the
871 Silurian record. Journal of the Geological Society 147, 663–674.
872 https://doi.org/10.1144/gsjgs.147.4.0663

873 Jeppsson, L., Aldridge, R.J., 2000. Ludlow (late Silurian) oceanic episodes and events.
874 Journal of the Geological Society 157, 1137–1148. https://doi.org/10.1144/jgs.157.6.1137

875 Jeppsson, L., Aldridge, R.J., Dorning, K.J., 1995. Wenlock (Silurian) oceanic episodes
876 and events. Journal - Geological Society (London) 152, 487–498.
877 https://doi.org/10.1144/gsjgs.152.3.0487

878 Jeppsson, L., Talent, J.A., Mawson, R., Simpson, A.J., Andrew, A.S., Calner, M.,
879 Whitford, D.J., Trotter, J.A., Sandström, O., Caldon, H.J., 2007. High-resolution Late
880 Silurian correlations between Gotland, Sweden, and the Broken River region, NE
881 Australia: Lithologies, conodonts and isotopes. Palaeogeography, Palaeoclimatology,
882 Palaeoecology 245, 115–137. https://doi.org/10.1016/j.palaeo.2006.02.032

883 Kiipli, T., Kiipli, E., Kaljo, D., 2010. Silurian sea level variations estimated using SiO2/Al2O
884 3 and K2O/A12O3 ratios in the Priekule drill core section, Latvia. Bollettino della Societa
885 Paleontologica Italiana 49, 55–63.

886 Kozłowski, W., Sobień, K., 2012. Mid-Ludfordian coeval carbon isotope, natural gamma
887 ray and magnetic susceptibility excursions in the Mielnik IG-1 borehole (Eastern Poland)-
888 Dustiness as a possible link between global climate and the Silurian carbon isotope
889 record. Palaeogeography, Palaeoclimatology, Palaeoecology 339–341, 74–97.
890 https://doi.org/10.1016/j.palaeo.2012.04.024

Kříž, J., 1992. Silurian field excursions: Prague Basin (Barrandian), Bohemia. National Museum of Wales.

Kříž, J., 1991. The Silurian of the Prague Basin (Bohemia)–tectonic, eustatic and volcanic controls on facies and faunal development. Special Papers in Palaeontology 44, 179–203.

Laskar, J., 2020. Astrochronology, in: Geologic Time Scale 2020. Elsevier, pp. 139–158. https://doi.org/10.1016/B978-0-12-824360-2.00004-8

Laskar, J., Robutel, P., Joutel, F., Gastineau, M., Correia, A.C.M., Levrard, B., 2004. A long-term numerical solution for the insolation quantities of the Earth. Astronomy and Astrophysics 428, 261–285. https://doi.org/10.1051/0004-6361:20041335

Laurin, J., Meyers, S.R., Uličný, D., Jarvis, I., Sageman, B.B, 2015. Axial obliquity control on the greenhouse carbon budget through middle- to high-latitude reservoirs. Paleoceanography 30, 133–149. https://doi.org/10.1002/2014PA002736

Laurin, J., Růžek, B., Giorgioni, M., 2017. Astronomical Signals in Carbon Isotopes: Phase Distortion as a Signature of the Carbon Cycle. Paleoceanography 32, 1236–1255. https://doi.org/10.1002/2017PA003143

Lehnert, O., Frýda, J., Buggisch, W., Munnecke, A., Nützel, A., Kříž, J., Manda, S., 2007. δ13C records across the late Silurian Lau event: New data from middle palaeo-latitudes of northern peri-Gondwana (Prague Basin, Czech Republic). Palaeogeography, Palaeoclimatology, Palaeoecology 245, 227–244. https://doi.org/10.1016/j.palaeo.2006.02.022

912 Lehnert, O., Eriksson, M.E., Calner, M., Joachimski, M. and Buggisch, W., 2007.
913 Concurrent sedimentary and isotopic indications for global climatic cooling in the Late
914 Silurian. Acta Palaeontol. Sin. 46, 249-255

915 Li, M., Hinnov, L.A., Huang, C., Ogg, J.G., 2018. Sedimentary noise and sea levels linked
916 to land-ocean water exchange and obliquity forcing. Nature Communications 9.
917 https://doi.org/10.1038/s41467-018-03454-y

918 Li, M., Li, X., Hesselbo, S.P., Li, M., Liu, W., Wu, W., Pan, J., Gao, R., 2024. Astronomical
919 pacing and secular evolution of lake-level changes reconstructed by sedimentary noise
920 modelling during the Early Jurassic icehouses-(super)greenhouses. Science China Earth
921 Sciences 67, 252–267. https://doi.org/10.1007/s11430-023-1187-8

922 Li, Z.H., Guo, Z., Chen, Z.Q., Poulton, S.W., Bao, Y., Zhao, L., Zhang, F.F., 2021. A novel
923 carbon cycle turbulence index identifies environmental and ecological perturbations.
924 Geochemical Perspectives Letters 20, 11–15. https://doi.org/10.7185/geochemlet.2137

925 Lourens, L.J., Hilgen, F.J., 1997. Long-periodic variations in the earth's obliquity and their
926 relation to third-order eustatic cycles and late Neogene glaciations. Quaternary
927 International 40, 43–52. https://doi.org/10.1016/S1040-6182(96)00060-2

928 Ma, W., Tian, J., Li, Q., Wang, P., 2011. Simulation of long eccentricity (400-kyr) cycle in
929 ocean carbon reservoir during Miocene Climate Optimum: Weathering and nutrient
930 response to astronomical change. Geophysical Research Letters 38.
931 https://doi.org/10.1029/2011GL047680

Manda, Š., Kříž, J., 2006. Environmental and biotic changes in subtropical isolated carbonate platforms during the Late Silurian Kozlowskii Event, Prague Basin. GFF 128, 161–168.https://doi.org/10.1080/11035890601282161

Marsaglia, K.M., Browne, G.H., George, S.C., Kemp, D.B., Jaeger, J.M., Carson, D., Richaud, M., IODP Expedition 317 Scientific Party, 2017. The Transformation of Sediment Into Rock: Insights From IODP Site U1352, Canterbury Basin, New Zealand. Journal of Sedimentary Research 87, 272–287. https://doi.org/10.2110/jsr.2017.15

Martinez, M., 2018. Mechanisms of Preservation of the Eccentricity and Longer-term Milankovitch Cycles in Detrital Supply and Carbonate Production in Hemipelagic Marl-Limestone Alternations, Stratigraphy & Timescales. Elsevier Ltd. https://doi.org/10.1016/bs.sats.2018.08.002

Martinez, M., Aguirre-Urreta, B., Dera, G., Lescano, M., Omarini, J., Tunik, M., O'Dogherty, L., Aguado, R., Company, M., and Bodin, S., 2023, Synchrony of carbon cycle fluctuations, volcanism and astronomical forcing during the Early Cretaceous: Earth-Science Reviews, v. 239, doi:10.1016/j.earscirev.2023.104356.

Melchin, M.J., Sadler, P.M., Cramer, B.D., 2020. The Silurian Period, Geologic Time Scale 2020. BV. https://doi.org/10.1016/B978-0-12-824360-2.00021-8

Mergl, M., Frýda, J., Kubajko, M., 2018. Response of organophosphatic brachiopods to the mid-Ludfordian (late Silurian) carbon isotope excursion and associated extinction events in the Prague Basin (Czech Republic). Bulletin of Geosciences 93(3), 369–400. https://doi.org/10.3140/bull.geosci.1710

954 Meyers, S.R., 2019. Cyclostratigraphy and the problem of astrochronologic testing. Earth-
955 Science Reviews 190, 190–223. https://doi.org/10.1016/j.earscirev.2018.11.015

956 Meyers, S.R., 2015. The evaluation of eccentricity-related amplitude modulation and
957 bundling in paleoclimate data: An inverse approach for astrochronologic testing and time
958 scale optimization. Paleoceanography 30, 1625–1640.
959 https://doi.org/10.1002/2015PA002850

960 Munnecke, A., Calner, M., Harper, D.A.T., Servais, T., 2010. Ordovician and Silurian sea
961 – water chemistry , sea level , and climate : A synopsis. Palaeogeography,
962 Palaeoclimatology, Palaeoecology 296, 389–413.
963 https://doi.org/10.1016/j.palaeo.2010.08.001

964 Munnecke, A., Samtleben, C., Bickert, T., 2003. The Ireviken Event in the lower Silurian
965 of Gotland, Sweden - Relation to similar Palaeozoic and Proterozoic events.
966 Palaeogeography, Palaeoclimatology, Palaeoecology 195, 99–124.
967 https://doi.org/10.1016/S0031-0182(03)00304-3

968 Mutterlose, J., Ruffell, A., 1999. Milankovitch-scale palaeoclimate changes in pale-dark
969 bedding rhythms from the Early Cretaceous (Hauterivian and Barremian) of eastern
970 England and northern Germany. Palaeogeography, Palaeoclimatology, Palaeoecology
971 154, 133–160. https://doi.org/10.1016/S0031-0182(99)00107-8

972 Ohkouchi, N., Kuroda, J., Taira, A., 2015. The origin of Cretaceous black shales: A
973 change in the surface ocean ecosystem and its triggers. Proceedings of the Japan
974 Academy Series B: Physical and Biological Sciences 91, 273–291.
975 https://doi.org/10.2183/pjab.91.273

976 Pohl, A., Lu, Z., Lu, W., Stockey, R.G., Elrick, M., Li, M., Desrochers, A., Shen, Y., He,
977 R., Finnegan, S., Ridgwell, A., 2021. Vertical decoupling in Late Ordovician anoxia due
978 to reorganization of ocean circulation. Nature Geoscience 14, 868–873.
979 https://doi.org/10.1038/s41561-021-00843-9

980 Pohl, A., Ridgwell, A., Stockey, R.G., Thomazo, C., Keane, A., Vennin, E., Scotese, C.R.,
981 2022. Continental configuration controls ocean oxygenation during the Phanerozoic.
982 Nature 608, 523–527. https://doi.org/10.1038/s41586-022-05018-z

983 Saltzman, M.R., 2005. Phosphorus, nitrogen, and the redox evolution of the Paleozoic
984 oceans. Geology 33, 573–576. https://doi.org/10.1130/G21535.1

985 Scotese, C.R., 2021. An atlas of phanerozoic paleogeographic maps: The seas come in
986 and the seas go out. Annual Review of Earth and Planetary Sciences 49, 679–728.
987 https://doi.org/10.1146/annurev-earth-081320-064052

988 Sproson, A.D., 2020. Pacing of the latest Ordovician and Silurian carbon cycle by a 4.5
989 Myr astronomical cycle. Palaeogeography, Palaeoclimatology, Palaeoecology 540,
990 109543. https://doi.org/10.1016/j.palaeo.2019.109543

991 Sproson, A.D., Pogge von Strandmann, P.A.E., Selby, D., Jarochowska, E., Frýda, J.,
992 Hladil, J., Loydell, D.K., Slavík, L., Calner, M., Maier, G., Munnecke, A., Lenton, T.M.,
993 2022. Osmium and lithium isotope evidence for weathering feedbacks linked to
994 astronomically paced organic carbon burial and Silurian glaciations. Earth and Planetary
995 Science Letters 577. https://doi.org/10.1016/j.epsl.2021.117260

996 Štorch, P., 1995. Biotic crises and post-crisis recoveries recorded by Silurian planktonic
997 graptolite faunas of the Barrandian area (Czech Republic). Geolines 3, 59–70.

998 Tasáryová, Z., Schnabl, P., Čížková, K., Pruner, P., Janoušek, V., Rapprich, V., Štorch,
999 P., Manda, Š., Frýda, J., Trubač, J., 2014. Gorstian palaeoposition and geotectonic
1000 setting of Suchomasty Volcanic Centre (Silurian, Prague Basin, Teplá-Barrandian Unit,
1001 Bohemian Massif). Gff 136, 262–265. https://doi.org/10.1080/11035897.2013.879735

1002 Tonarová, P., Frýda, J., Kubajko, M., Hints, O., 2025. Response of the jawed polychaete
1003 fauna to the mid-Ludfordian (late Silurian) carbon isotope excursion and associated
1004 extinction events in the Prague Basin (Czech Republic). Bulletin of Geosciences 100(4).
1005 https://doi.org/10.3140/bull.geosci.1913

1006 Trotter, J.A., Williams, I.S., Barnes, C.R., Männik, P., Simpson, A.J., 2016. New conodont
1007 δ18O records of Silurian climate change: Implications for environmental and biological
1008 events. Palaeogeography, Palaeoclimatology, Palaeoecology 443, 34–48.
1009 https://doi.org/10.1016/j.palaeo.2015.11.011

1010 Vervoort, P., Turner, S.K., Rochholz, F., Ridgwell, A., 2024. Earth system model analysis
1011 of how astronomical forcing is imprinted onto the marine geological record: The role of
1012 the inorganic (carbonate) carbon cycle and feedbacks. Paleoceanography and
1013 Paleoclimatology 39. https://doi.org/10.1029/2023PA004826

1014 Vervoort, P., Kirtland Turner, S., Hülse, D., Greene, S. E., & Ridgwell, A., 2026. Earth
1015 system model analysis of how astronomical forcing is imprinted onto the marine
1016 geological record: The role of the marine organic carbon cycle and

feedbacks. *Paleoceanography and Paleoclimatology*, 41, e2025PA005181. https://doi.org/10.1029/2025PA005181

Waltham, D., 2015. Milankovitch Period Uncertainties and Their Impact on Cyclostratigraphy. Journal of Sedimentary Research 85, 990–998. https://doi.org/10.2110/jsr.2015.66

Westerhold, T., Marwan, N., Drury, A.J., Liebrand, D., Agnini, C., Anagnostou, E., Barnet, J.S., Bohaty, S.M., De Vleeschouwer, D., Florindo, F. and Frederichs, T., 2020. An astronomically dated record of Earth's climate and its predictability over the last 66 million years. science, 369(6509), pp.1383-1387. https://doi.org/10.1126/science.aba6853

Wu, Y., Malinverno, A., Meyers, S.R., Hinnov, L.A., 2024. A 650-Myr history of Earth's axial precession frequency and the evolution of the Earth-Moon system derived from cyclostratigraphy. Science Advances 10, eado2412.https://doi.org/10.1126/sciadv.ado2412

Zeebe, R.E., Ridgwell, A., 2011. Past changes in ocean carbonate chemistry, in: Ocean Acidification. Oxford University Press. https://doi.org/10.1093/oso/9780199591091.003.0007

Zeeden, C., Meyers, S.R., Lourens, L.J., and Hilgen, F.J., 2015, Testing astronomically tuned age models: Paleoceanography, v. 30, p. 369–383, https://doi.org/10.1002/2014PA002762.

Zhang, F., Frýda, J., Mojtaba F., Yi-bo L., Guangyi W., Mengchun C., Na L., Jianlin Zh., Frýdová, B., Haizhen W., Shuzhong Sh., 2022. Marine anoxia as a trigger for the largest

1038 Phanerozoic positive carbon isotope excursion: evidence from carbonate barium isotope
1039 records. – Earth and Planetary Science Letters, 584.
1040 https://doi.org/10.1016/j.epsl.2022.117421

1041 Zhao, X., Xue, N., Yang, H., Zheng, D., Peng, J., Frieling, J. , De Vleeschouwer, D., Fu,
1042 X., Jia, W., Fang, Y., Li, S., Wang, M., Zhao, X., Wang, Q., Zhang, H., Sha, J., Jenkyns,
1043 H., Claeys, P. (2025). Climate–carbon-cycle interactions and spatial heterogeneity of the
1044 late Triassic Carnian pluvial episode. Nature Communications. 16.
1045 https://doi.org/10.1038/s41467-025-61262-7.